

# EC 22536–5304: A lead-rich and metal-poor long-period binary

M. Dorsch<sup>1,2</sup>, C. S. Jeffery<sup>3</sup>, A. Irrgang<sup>1</sup>, V. Woolf<sup>4</sup>, U. Heber<sup>1</sup>

<sup>1</sup> Dr. Karl Remeis-Observatory & ECAP, Friedrich-Alexander University Erlangen-Nürnberg, Sternwartstr. 7, 96049 Bamberg, Germany e-mail: matti.dorsch@fau.de

<sup>2</sup> Institut für Physik und Astronomie, Universität Potsdam, Haus 28, Karl-Liebknecht-Str. 24/25, 14476 Potsdam-Golm, Germany

<sup>3</sup> Armagh Observatory and Planetarium, College Hill, Armagh BT61 9DG, Northern Ireland

<sup>4</sup> Department of Physics, University of Nebraska at Omaha, 6001 Dodge St, Omaha, NE 68182-0266, USA

Received ; accepted

## ABSTRACT

Helium-burning hot subdwarf stars of spectral types O and B (sdO/B) are thought to be produced through various types of binary interactions. The helium-rich hot subdwarf star EC 22536–5304 was recently found to be extremely enriched in lead. Here, we show that EC 22536–5304 is a binary star with a metal-poor subdwarf F-type (sdF) companion. We performed a detailed analysis of high-resolution SALT/HRS and VLT/UVES spectra, deriving metal abundances for the hot subdwarf, as well as atmospheric parameters for both components. Because we consider the contribution of the sdF star, the derived lead abundance for the sdOB,  $+6.3 \pm 0.3$  dex relative to solar, is even higher than previously thought. We derive  $T_{\text{eff}} = 6210 \pm 70$  K,  $\log g = 4.64 \pm 0.10$ ,  $[\text{Fe}/\text{H}] = -1.95 \pm 0.04$ , and  $[\alpha/\text{Fe}] = +0.40 \pm 0.04$  for the sdF component. Radial velocity variations, although poorly sampled at present, indicate that the binary system has a long orbital period of about 457 days. This suggests that the system was likely formed through stable Roche lobe overflow (RLOF). A kinematic analysis shows that EC 22536–5304 is on an eccentric orbit around the Galactic centre. This, as well as the low metallicity and strong alpha enhancement of the sdF-type companion, indicate that EC 22536–5304 is part of the Galactic halo or metal-weak thick disc. As the first long-period hot subdwarf binary at  $[\text{Fe}/\text{H}] \lesssim -1$ , EC 22536–5304 may help to constrain the RLOF mechanism for mass transfer from low-mass, low-metallicity red giant branch (RGB) stars to main-sequence companions.

**Key words.** stars: individual (EC 22536–5304) — subdwarfs — stars: abundances

## 1. Introduction

Hot subdwarf stars form a heterogeneous class of evolved stars located at the hot end of the horizontal branch or beyond (for reviews, see Heber 2009, 2016). This implies that they burn helium either in the core or in a shell, while their hydrogen envelope is very thin or almost absent. Accordingly, their masses are close to half that of the Sun. Most B-type subdwarf stars (sdB) have helium-poor atmospheres due to atmospheric diffusion (Hu et al. 2011; Michaud et al. 2011). In contrast, the hotter sdO stars are often found to be extremely enriched in helium. There is also an intermediate class of hot subdwarf stars, termed intermediate helium sdOB (iHe-sdOB). Their effective temperature and helium abundances are intermediate between the cooler helium poor sdBs and those of the hotter helium-rich sdO stars (e.g. Németh et al. 2012; Jeffery et al. 2021). Recently, several members of this small population have been found to be extremely enriched in heavy elements such as strontium, yttrium, zirconium, or lead (e.g. Naslim et al. 2011; Jeffery et al. 2017; Dorsch et al. 2020). The hot component of EC 22536–5304 was identified as an extremely lead-rich iHe-sdOB by Jeffery & Miszalski (2019); in fact, it is the most lead-rich star known to date. Like the depletion of helium observed in the photospheres of most sdB stars, the strong enrichment in heavy metals is usually attributed to diffusion and selective radiative acceleration. However, quantitative predictions are still lacking for atomic diffusion in the atmospheres of iHe-sdOB stars.

A close inspection of new high-resolution spectra taken with SALT/HRS reveals a second component in the spectrum of EC 22536–5304: a metal-poor, subdwarf-F-type (sdF) main-

sequence (MS) star, which was not considered in the previous analysis. Many helium-poor sdB stars are found in binary systems with low-mass MS stars or white dwarfs at short orbital periods of the order of ten days or fewer (Kupfer et al. 2015). They are thought to be formed following a common envelope (CE) phase, in which the red giant progenitor to the sdB has lost most of its hydrogen-rich envelope, just before it ignites helium burning in the core (Han et al. 2002).

The orbital properties of all 23 solved helium-poor sdB stars in long-period binaries have recently been published by Vos et al. (2019). They find that the orbital periods of these sdB + F/G/K-type systems range from about 500 to 1400 days. The hot subdwarf stars in such systems are the result of a stable Roche overflow (RLOF) as the progenitor star to the sdB reaches the tip of the red giant branch (RGB, Han et al. 2003; Chen et al. 2013). Only two helium-rich subdwarf stars in long-period binary systems are known: the post-asymptotic giant branch (AGB) He-sdO HD 128220 B (Rauch 1993) and the He-sdO HD 113001 B, a visually resolved binary with a very long orbital period that has likely not undergone mass transfer (Tomley 1970; Goy 1980; Orlov et al. 2010). Very recently, Németh et al. (2021) have found the He-poor sdOB component of the long-period binary system SB 744 to be extremely enhanced in lead.

EC 22536–5304 is the first helium-rich heavy-metal subdwarf found to be in a binary system (long- or short-period). As we show in the following, EC 22536–5304 is likely to be a long-period binary, and the first such system found at a metallicity below about  $[\text{Fe}/\text{H}] = -1$ . It therefore presents a unique opportunity to study the RLOF evolutionary scenario, especially once

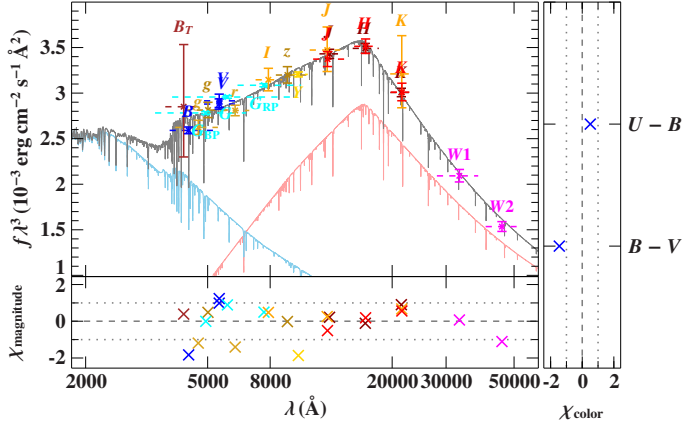


Fig. 1: Photometric fit for EC 22536–5304. Filter-averaged fluxes are shown as coloured data points that were converted from observed magnitudes. Filter widths are indicated by dashed horizontal lines. The grey line visualises the combined model spectrum while individual contributions are shown in blue (A) and red (B). The residual panels on the bottom and right side respectively show the differences between synthetic and observed magnitudes and colours. The following colour codes are used to identify the photometric systems: Tycho (brown, Høg et al. 2000), Johnson-Cousins (blue, Henden et al. 2015; Kilkenny et al. 2016), SDSS (yellow, Henden et al. 2015), SkyMapper (dark yellow, Wolf et al. 2018), *Gaia* (cyan, Riello et al. 2021), DENIS (orange, DENIS Consortium 2005), DES (bright yellow, Abbott et al. 2018), VISTA (dark red, McMahon et al. 2013), 2MASS (bright red, Cutri et al. 2003), and WISE (magenta, Cutri et al. 2021).

additional spectra become available that will further constrain the orbital parameters of the system.

In this paper, we present a detailed analysis of high-resolution spectra of EC 22536–5304. The presence of the cool component is confirmed by an analysis of the spectral energy distribution (SED), which is described in Sect. 2. The available spectroscopic data are summarised in Sect. 3. Results from the SED and spectroscopic analysis (Sect. 4) are combined with the parallax measurement provided by the *Gaia* mission to derive stellar masses, radii, and luminosities in Sect. 5. Because the cool companion (hereafter EC 22536–5304 B) contributes significantly in the optical range, we updated the metal abundances derived for the hot component (hereafter EC 22536–5304 A). A detailed account of the metal abundance analysis for the sdOB is given in Sect. 6. The radial velocities derived from the currently available spectra are used to perform a kinematic analysis in Sect. 7. The Galactic orbit of the system is characterised in Sect. 8. We summarise our results in Sect. 9.

## 2. Spectral energy distribution

Due to the large difference in their effective temperatures, both components of EC 22536–5304 are easily distinguished in the SED of the system. To obtain an initial estimate for the atmospheric parameters of both components, a first photometric fit was performed before the spectral analysis. We obtained apparent magnitudes from the ultraviolet to the infrared to construct the SED of EC 22536–5304. A general description of the  $\chi^2$  minimisation method used for the SED fit is given by Heber et al. (2018). In short, model spectra of both components were

Table 1: SED fit and spectroscopic fit results for the hot (A) and cool (B) components of EC 22536–5304.

	SED fit	Spectral fit
$\log \Theta_A$ (rad)	$-11.09^{+0.09}_{-0.05}$	–
$T_{\text{eff,A}}$ (K)	$38000^{+5000}_{-7000}$	$38000 \pm 400$
$\log g_A$		$5.81 \pm 0.04$
$\log n(\text{He})/n(\text{H})$		$-0.15 \pm 0.04$
$v_{\text{tb,A}}$ (km s $^{-1}$ )		$2.1 \pm 0.2$
$v_{\text{rot}} \sin i_A$ (km s $^{-1}$ )	–	$0.0^{+1.0}_{-0.0}$
$T_{\text{eff,B}}$ (K)	$6460^{+90}_{-190}$	$6210 \pm 70$
$\log g_B$		$4.64 \pm 0.10$
$[\text{Fe}/\text{H}]_B$		$-1.95 \pm 0.04$
$[\alpha/\text{Fe}]_B$		$+0.40 \pm 0.04$
$v_{\text{tb,B}}$ (km s $^{-1}$ )		$1.83 \pm 0.05$
$v_{\text{rot}} \sin i_B$ (km s $^{-1}$ )	–	$15.3 \pm 0.2$
Surface ratio	$34 \pm 9$	$34 \pm 5$

converted to filter-averaged magnitudes and scaled to match the observed magnitudes. Free fit parameters were the effective temperatures of both components, the angular diameter of the sdOB  $\Theta_A$ , and the surface ratio  $A_{\text{sdF}}/A_{\text{sdOB}}$ . Here, we used the same large model grids as for the spectroscopic analysis, which are described in Sect. 4. Interstellar reddening was considered as by Fitzpatrick et al. (2019), assuming an extinction parameter of  $R(55) = 3.02$ . Since no reliable UV magnitudes are available, we constrained the colour excess not to exceed the line-of-sight value given by Schlegel et al. (1998),  $E(B - V) = 0.126$  mag, which is reached in the fit. The first fit was later refined by fixing the helium abundance of the hot component, the metallicity and alpha enhancement of the cool component, and both surface gravities to values derived from the spectral analysis. The final SED fit is shown in Fig. 1. Table 1 compares results of the SED fit with parameters derived from the spectral fit (see Sect. 4).

Several heavy metal subdwarfs have been found to show peculiar low-amplitude photometric variability: the zirconium-rich LS IV–14° 116, Feige 46, and PHL 417 (Ahmad & Jeffery 2005; Latour et al. 2019b; Østensen et al. 2020), as well as the lead-rich UVO 0825+15 (Jeffery et al. 2017). It would therefore be interesting to search for photometric variability in EC 22536–5304 as well.

## 3. Spectroscopic observations

The spectroscopic data available for EC 22536–5304 are summarised in Table 2. EC 22536–5304 has been observed extensively with the Southern African Large telescope (SALT) using both the Robert Stobie Spectrograph (RSS) and the High Resolution Spectrograph (HRS). The setups used for both spectrographs are described in detail in Jeffery & Miszalski (2019). They used two long-slit RSS spectra taken in June 2018, as well as HRS spectra taken on 2017 May 18 and 2018 November 15, with exposure times of  $2 \times 2000$  s on both occasions. These individual HRS spectra have mean signal-to-noise ratios (S/N) of about 30. Twenty-one additional blue HRS spectra were taken between 2019 May 9 and 23, increasing the combined S/N to about 200. The HRS spectra consist of short échelle orders, which make order merging difficult. We used a technique

Table 2: Spectroscopic data available for EC 22536–5304<sup>a</sup>.

Spectrograph	Range / Å	$R$	$n_{\text{exp}}$	S/N
HRS/blue	3895 – 5520	43000	25	200
HRS/red	5500 – 8870	41000	9	120
RSS	3850 – 5100	1.6 Å <sup>b</sup>	2	100
UVES/blue	3740 – 4525	41000	3	50
UVES/red	5655 – 9463	42000	2	25

**Notes.** <sup>(a)</sup> The signal-to-noise ratio is the maximum reached in a combined spectrum. <sup>(b)</sup> The resolution for RSS is given as  $\Delta\lambda$ .

that normalises all orders simultaneously, ensuring continuity across the order overlaps, before stitching the individual orders together. Some residual anomalies persist, so we re-normalised the order-merged spectra before performing the spectral analysis. As a result, broad hydrogen and helium lines in these spectra could not be used to estimate atmospheric parameters. The HRS spectra remained essential for the detection of weak metal lines of both components, as well as the Mg I triplet. Coverage of the Mg I triplet is especially important because it is sensitive to the metallicity, alpha-enhancement, and surface gravity of the F-type companion.

In addition to the blue HRS spectra, nine red HRS spectra of sufficient quality are available. These spectra were taken on the same dates as the blue HRS spectra. Their near infrared coverage is especially useful since it includes the Ca II triplet of the F-type star, as well as He I 6678, 7065, and 7281 Å for the sdOB, all of which help to constrain the surface ratio.

We also make use of archival UVES spectra, which were obtained in October and December 2011 by M. R. Schreiber under Programme ID 088.D-0364(A). Because normalisation issues are less pronounced in the blue UVES spectra than in the HRS spectra, UVES spectra proved to be valuable for the determination of atmospheric parameters from broad hydrogen and helium lines, despite their lower S/N.

#### 4. Spectral analysis and atmospheric parameters

To model the contribution of the sdOB component, we used fully line-blanketed, plane-parallel, homogeneous, hydrostatic, non-local thermodynamic equilibrium (NLTE) synthetic spectra computed with TLUSTY and SYNSPEC, in particular the most recent public versions (for detailed descriptions, see Hubeny & Lanz 2017a,b,c). Heavy metals were included in LTE in the spectrum synthesis as described by Latour et al. (2019a). A first estimate of the atmospheric parameters was obtained using a large grid of synthetic spectra that was computed using the model atoms of Lanz & Hubeny (2003). This grid covers the full He-sdO/B parameter space in  $T_{\text{eff}}$ ,  $\log g$ , and helium abundance  $\log n(\text{He})/n(\text{H})$ . A smaller grid was then constructed around the best-fit parameters for the sdOB obtained with the first grid. To be consistent with the models used for the metal abundance analysis performed in Sect. 6, this second grid uses the largest model atoms distributed with TLUSTY 205. Because these model atoms include more energy levels, optical transitions that involve high-lying levels were treated in NLTE. The grid considers H, He, C, N, O, Ne, Mg, Al, Si, P, S, Ar, Ca, Fe, and Ni in NLTE at abundances close to those derived for the sdOB. The abundances of metals that could not be determined from the available spectra

(most importantly Fe and Ni) were set to the values derived for the iHe-sdOB HZ 44 (Dorsch et al. 2019).

Similarly, the cool companion was initially modelled using a large grid of model spectra. Here, we used LTE model atmospheres and synthetic spectra computed with ATLAS12 (Kurucz 1996) and SYNTH (Kurucz 1993). The initial grid extends from  $T_{\text{eff}} = 4000$  to 8000 K,  $\log g = 2.0$  to 5.2,  $[\text{Fe}/\text{H}] = -2.0$  to +0.5 dex, and covers microturbulent velocities of  $v_{\text{tb}} = 0, 1$ , and 2 km s<sup>-1</sup>. A solar helium abundance was assumed. The F-type companion is metal poor ( $[\text{Fe}/\text{H}] = -1.9$ ) and strongly alpha-enhanced, which is typical for halo stars (e.g. Fuhrmann 1998). The initial grid was therefore computed using a fixed alpha enhancement of  $[\alpha/\text{Fe}] = 0.4$  dex relative to the photospheric solar values of Asplund et al. (2009). As for the sdOB component, a second, smaller grid was constructed around the best-fit parameters. This grid also uses ATLAS12 and SYNTH model spectra, but it was additionally allowed to vary in alpha enhancement. The dimensions of all four grids of synthetic spectra used in this analysis are summarised in Table A.1.

It is challenging to determine the surface gravity of the F-type companion accurately. The wings of hydrogen lines, which are typically used to determine the surface gravity of sdB stars, are less useful for F-type stars because they are less sensitive to the density and correlate strongly with temperature. In EC 22536–5304, this is further complicated by the contribution of the sdOB, which has very broad hydrogen lines. The strength of the bluest Balmer and Paschen lines is sensitive to the surface gravity due to level dissolution. Unfortunately, our spectra lack coverage of these high Balmer lines, while the high Paschen lines are below the detection limit. The observed Balmer series, from  $H_{\alpha}$  up to  $H_{11}$ , excludes surface gravities  $\log g_{\text{B}} < 4.0$ . Instead, the surface gravity of cool (F/G-type) stars is often derived from the Fe I-II ionisation equilibrium, which also depends on the effective temperature. The strengths of the Mg I triplet and the Ca II 3934, 3968 Å resonance lines are sensitive to the surface gravity and the respective abundances. As shown in Fig. 2, the Mg I triplet in EC 22536–5304 is well reproduced at  $\log g_{\text{B}} = 4.7$ , assuming an alpha enhancement of 0.4 dex.

We performed global spectral fits in order to consider all sensitive absorption lines in the observed spectra. Examples for strong hydrogen, helium, and calcium lines are shown in Fig. 3. The atmospheric parameters of both components and the surface ratio were varied simultaneously. The individual UVES and HRS exposures were not stacked but evaluated at the same time. This is necessary because the radial velocity difference between both components is not constant over more than a few days. Spectral regions that were not well reproduced were removed before performing the final fit. This includes metal lines with uncertain atomic data, as well as the cores of Ca II resonance and hydrogen Balmer lines, which are poorly modelled in our LTE models for the cool component. After a first fit using large model grids, a second global fit was performed that used tailored grids for both components, as described above.

The atmospheric parameters derived from the final spectral fit are listed in Table 1. They are consistent with the results obtained from the SED fit in Sect. 2, but more precise. We use 1- $\sigma$  intervals for the statistical uncertainties. Due to the high resolution and high total S/N of our spectra, purely statistical uncertainties are small. The total uncertainties are dominated by systematic effects, such as deficiencies in the synthetic spectra or limited accuracy in the normalisation of our spectra. We estimate systematic uncertainties of 1% in  $T_{\text{eff}}$ , as well as 0.04 in  $\log g_{\text{A}}$ ,  $\log n(\text{He})/n(\text{H})$ ,  $[\text{Fe}/\text{H}]_{\text{B}}$ , and  $[\alpha/\text{Fe}]_{\text{B}}$ . These systematic uncertainties were added in quadrature to the smaller statistical errors.

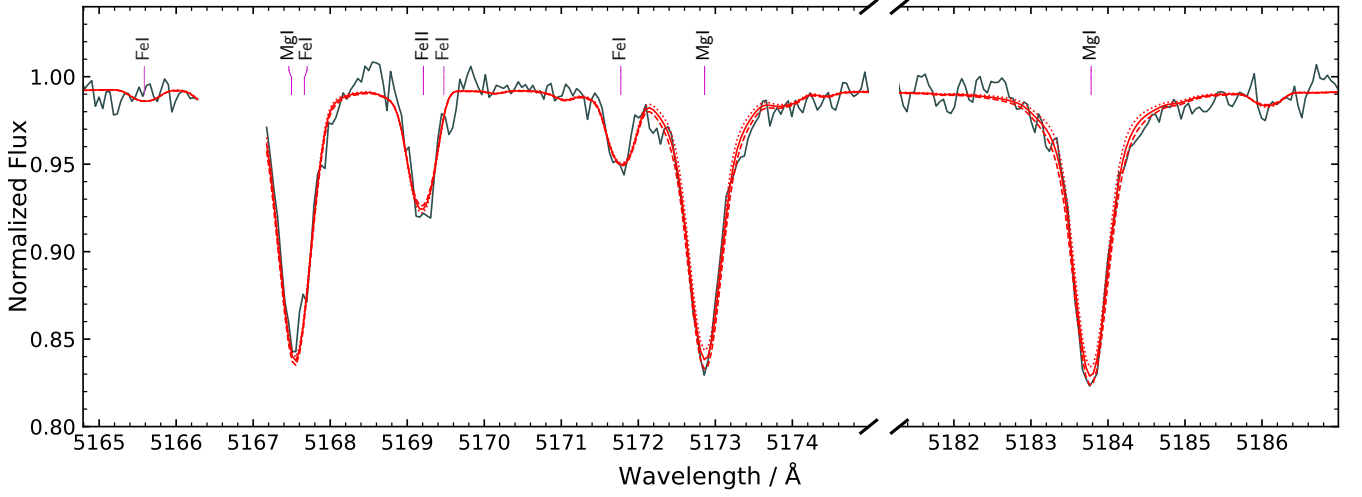


Fig. 2: Mg I triplet in the HRS spectrum of EC 22536–5304 (grey). The combined model spectrum (red) is the sum of the contributions of the sdOB and F-type star at the best fit. The dashed spectrum was computed at  $\log g_2 = 4.9$ , while the dotted spectrum uses  $\log g_2 = 4.55$ .

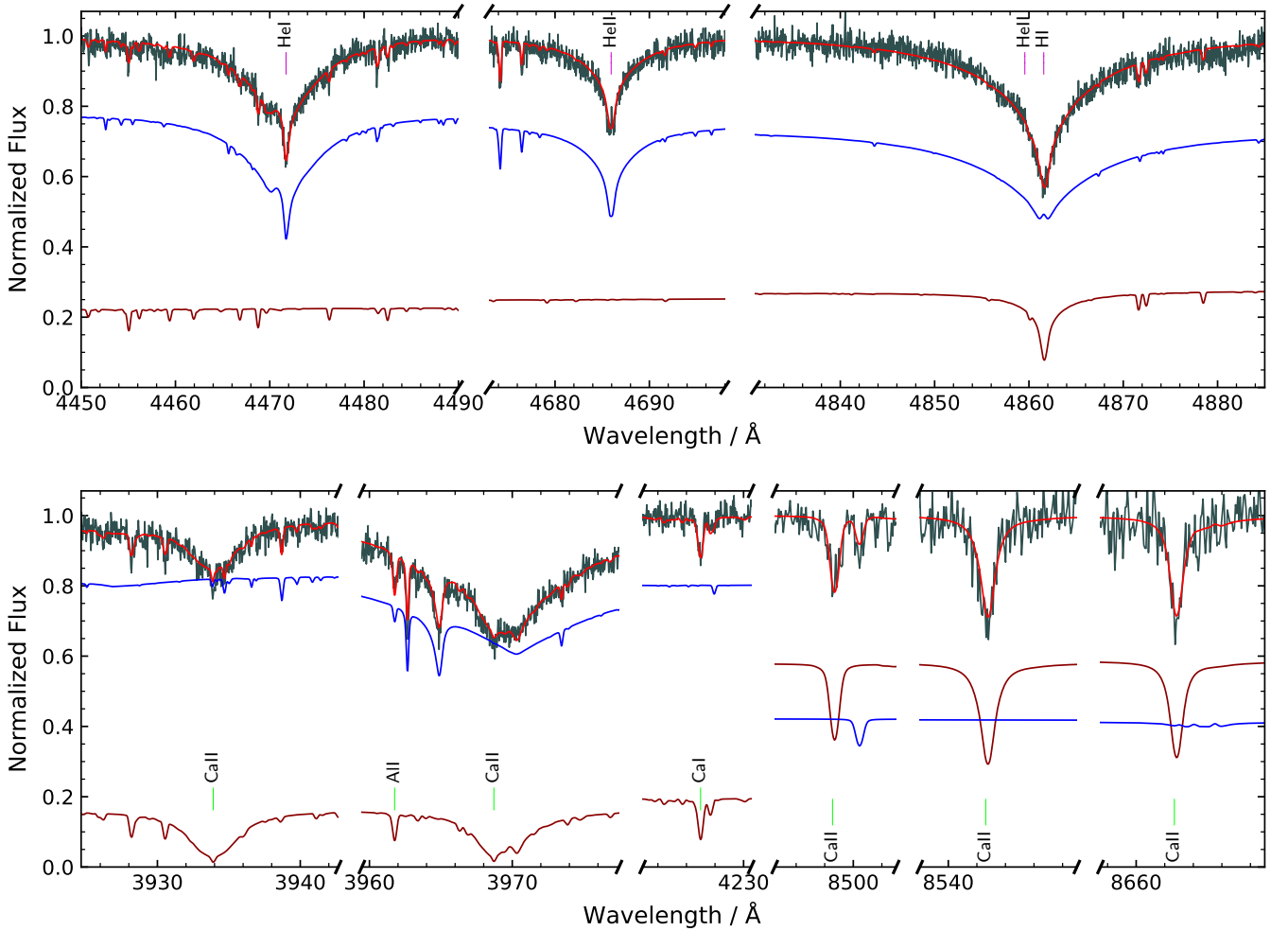


Fig. 3: Top: Examples of prominent helium and hydrogen lines in an individual UVES spectrum of EC 22536–5304 (grey). The combined model spectrum (red) is the sum of the contributions of the sdOB (blue) and F-type star (dark red). Bottom: Similarly, the strongest calcium lines in blue and red UVES spectra.



Table 3: Stellar parameters for EC 22536–5304 as derived by combining the SED, spectroscopic, and parallax measurements. The mode and the highest density interval of each quantity are given for 1- $\sigma$  probability (see Bailer-Jones et al. 2018).

	A	B
$R/R_{\odot}$	$0.132 \pm 0.007$	$0.75 \pm 0.07$
$M/M_{\odot}$	$0.40 \pm 0.06$	$0.84^{+0.29}_{-0.23}$
$L/L_{\odot}$	$32 \pm 4$	$0.74^{+0.15}_{-0.14}$

We used a higher systematic uncertainty of 0.10 dex for the surface gravity of the cool component,  $\log g_B$ , for two reasons. First, there is no spectral feature that is strongly dependent on  $\log g_B$ . Second,  $\log g_B$  is strongly correlated with other free parameters such as  $T_{\text{eff},B}$ , the surface ratio, and the alpha enhancement.

We find a significant projected rotational velocity of  $15.3 \pm 0.2 \text{ km s}^{-1}$  for the sdF-type companion. This rotation is relatively slow compared to the values Vos et al. (2018) found for the cool companions in their sample of nine long-period sdB + F/G/K-type systems. EC 22536–5304 A is consistent with no rotation, which is not unusual since most hot subdwarfs are slow rotators, including stars found in wide binaries (Geier & Heber 2012).

## 5. Mass, radius, and luminosity

Stellar parameters can be derived using the precise parallax measurement provided by the Early Data Release 3 (EDR3) of the *Gaia* mission (Gaia Collaboration et al. 2016, 2021),  $\varpi = 1.40 \pm 0.04 \text{ mas}$ . We corrected the parallax for its zero-point offset following Lindegren et al. (2021) and inflated the corresponding uncertainty using the function suggested by El-Badry et al. (2021). Stellar radii are then given as  $R = \Theta / (2\varpi)$ . Here,  $\Theta$  refers to the individual angular diameters determined from the SED. In contrast to the SED fit performed in Sect. 2, the angular diameter used here,  $\log \Theta_A / \text{rad} = -11.078^{+0.018}_{-0.022}$ , was obtained while keeping all atmospheric parameters fixed to the more precise spectroscopic values as listed in Table 1. Combining the radii with the spectroscopic surface gravities then allowed us to derive the stellar masses  $M = gR^2/G$ , where  $G$  is the gravitational constant. Stellar luminosities are given as  $L/L_{\odot} = (R/R_{\odot})^2 (T_{\text{eff}}/T_{\text{eff},\odot})^4$ . The stellar parameters for both components are listed in Table 3. We used a Monte Carlo method to propagate the uncertainties.

Due to the high uncertainty in surface gravity and surface ratio, the mass for the sdF component is poorly constrained. As discussed in Sect. 7, it is likely that the EC 22536–5304 system formed through Roche-lobe overflow. However, the transferred mass is expected to be less than  $0.03 M_{\odot}$  (Vos et al. 2018). It is likely that the transferred mass for EC 22536–5304 B is significantly below this value, given its relatively slow projected rotation. We can therefore derive an evolutionary mass for the sdF based on its spectroscopic effective temperature and surface gravity. Figure 4 shows single-star evolutionary tracks from the MIST project (Choi et al. 2016) for metallicities of  $[\text{Fe}/\text{H}] = -1.9 \pm 0.3$ . In the Kiel diagram (Fig. 4; upper panel), our atmospheric parameters of EC 22536–5304 B are consistent with masses between about  $0.8$  and  $0.7 M_{\odot}$ . We cannot estimate an evolutionary age directly from the atmospheric parameters since our surface gravity puts EC 22536–5304 B close to the predicted zero-age MS. Given the low metallicity of EC 22536–5304 B, one would expect an age of the order of

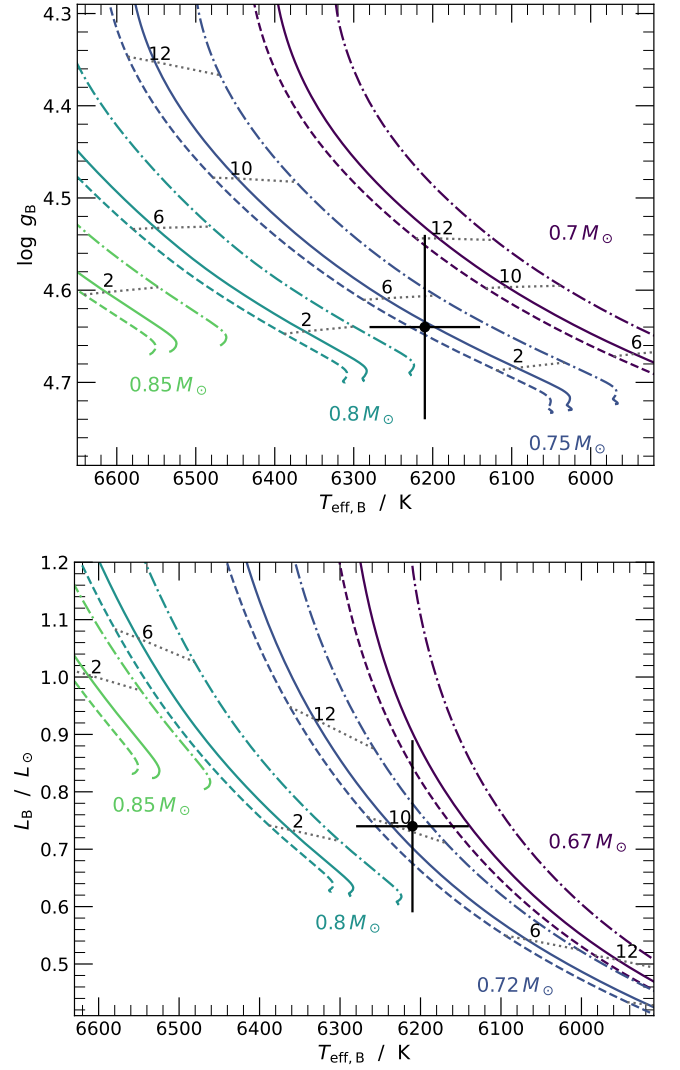


Fig. 4: Main-sequence evolutionary tracks from MIST (Choi et al. 2016) for  $[\text{Fe}/\text{H}] = -2.1$  (dashed),  $-1.9$  (solid), and  $-1.6$  (dash-dotted), as well as for four initial masses. The upper panel shows the Kiel diagram, while the Hertzsprung-Russell diagram is shown in the lower panel. The dotted grey lines indicate equal age and are labelled in Gyr. The parameters of EC 22536–5304 B and their uncertainties are marked by the cross.

about 10 Gyr or more. The spectroscopic surface gravity for the sdF may therefore be slightly overestimated.

It is useful to consider the position of EC 22536–5304 B in the Hertzsprung-Russell diagram (luminosity vs.  $T_{\text{eff}}$ ), given that the luminosity is (almost) independent of the spectroscopic surface gravity. As shown in the bottom panel of Fig. 4, our estimates for the luminosity and effective temperature of the sdF are consistent with a lower evolutionary mass, about  $0.7 M_{\odot}$ . While this mass would be consistent with the expected age, the uncertainties are large.

It is not possible to directly derive an evolutionary mass for the sdOB because too many evolutionary tracks cross its position in the  $T_{\text{eff}} - \log g$  plane. However, the mass expected for a sdOB that was formed through RLOF is close to the core mass that is required for the helium-flash at the top of the RGB, or about  $0.49 M_{\odot}$  at  $[\text{Fe}/\text{H}] \approx -2$  (Dorman et al. 1993). Although

Table 4: Metal abundance results for EC 22536–5304 A by number fraction ( $\log \epsilon = \log n_X / \sum_i n_i$ ) and number fraction relative to solar ( $\log \epsilon / \epsilon_\odot$ , [Asplund et al. 2009](#)). The number of resolved lines used per ionisation stage is given in the last column (with equivalent widths  $> 10$  mÅ).

Element	$\log \epsilon$	$\log \epsilon / \epsilon_\odot$	$N_{\text{lines}}$
C II-IV	$-2.88 \pm 0.20$	$0.73 \pm 0.21$	19/45/2
N II-III	$-3.73 \pm 0.20$	$0.48 \pm 0.21$	22/9
O II-III	$-3.46 \pm 0.20$	$-0.11 \pm 0.21$	46/4
Mg II	$-5.07 \pm 0.30$	$-0.64 \pm 0.30$	1
Si III-IV	$-5.52 \pm 0.25$	$-0.99 \pm 0.25$	1/2
P III-IV	$-5.92 \pm 0.30$	$0.70 \pm 0.30$	1/1
S III-IV	$-5.76 \pm 0.30$	$-0.84 \pm 0.30$	1/1
Ar	$< -5.80^{+0.40}$	$< -0.17^{+0.41}$	
Ca	$< -5.42^{+0.40}$	$< 0.27^{+0.40}$	
Ti	$< -5.84^{+0.50}$	$< 1.24^{+0.50}$	
Fe	$< -4.30^{+0.30}$	$< 0.23^{+0.30}$	
Zn	$< -5.36^{+0.40}$	$< 2.11^{+0.40}$	
Ga	$< -5.82^{+0.40}$	$< 3.18^{+0.40}$	
Ge	$< -5.89^{+0.40}$	$< 2.50^{+0.40}$	
Kr	$< -4.89^{+0.40}$	$< 3.90^{+0.40}$	
Sr	$< -5.27^{+0.40}$	$< 3.90^{+0.40}$	
Y	$< -5.76^{+0.40}$	$< 4.07^{+0.40}$	
Zr	$< -6.71^{+0.40}$	$< 2.75^{+0.40}$	
Sn	$< -6.44^{+0.40}$	$< 3.56^{+0.40}$	
Pb III-IV	$-4.01 \pm 0.30$	$6.27 \pm 0.32$	5/7

higher than the  $0.40 \pm 0.06 M_\odot$  found for EC 22536–5304 A, the lower value observed is still consistent with it being a core helium burning star.

## 6. Metal abundance analysis

The atmospheric parameters of both components were kept fixed for the metal abundance analysis. The spectrum of the cool companion was modelled using ATLAS12/SYNTH using the final best-fit atmospheric parameters. We used the global  $\chi^2$  fitting procedure developed by [Irrgang et al. \(2014\)](#) to simultaneously determine the abundances for all metals that show sufficiently strong lines in the hot component (C, N, O, Mg, Si, P, Pb). A grid of synthetic spectra that include lines of one metal only was computed for each metal using SYNSPEC, always based on the same TLUSTY atmosphere. This model atmosphere was calculated for the best-fit atmospheric parameters derived in Sect. 4. To allow an estimation of the microturbulent velocity, each grid was calculated for microturbulent velocities of 0 and 3 km s<sup>-1</sup>. The full synthetic spectrum was then constructed by multiplication of all individual metal spectra, which were interpolated to the desired abundances. This method is well tested for sdB and other B-type stars (e.g. [Schaffenroth et al. 2021](#); [Irrgang et al. 2020](#)). It assumes that small changes in the metal abundances do not influence the atmospheric structure and that there are few intrinsic blends between lines of different metals. The abundance fitting procedure was repeated using a TLUSTY atmosphere that consistently includes the abundances from a first fit. As before, spectral regions that were not well reproduced were removed from the fit.

Because the observed lines that originate from the sdOB component show no strong signs of a microturbulent velocity,

Table 5: Lead lines detected in the spectrum of EC 22536–5304. References for the oscillator strengths are stated in the last column.

Ion	$\lambda / \text{\AA}$	$\log gf$	Ref.
Pb III	3854.080	+0.302	1
Pb III	4272.660	-0.462	1
Pb III	4571.219	+0.029	1
Pb III	4761.120	+0.012	1
Pb III	4798.590	-0.356	1
Pb IV	3962.467	-0.047	2
Pb IV	4049.832	-0.065	2
Pb IV	4174.478	-0.444	3
Pb IV	4496.223	-0.437	3
Pb IV	4534.447	+1.190	3
Pb IV	4534.917	+1.102	3
Pb IV	4605.400	-0.991	3

**Notes.** (1) [Alonso-Medina et al. \(2009\)](#); (2) [Safronova & Johnson \(2004\)](#); (3) [Alonso-Medina et al. \(2011\)](#).

the best-fit  $v_{\text{t,b,A}} = 2.1 \pm 0.2$  km s<sup>-1</sup> can be considered as an upper limit. The final abundance pattern for EC 22536–5304 A is listed in Table 4 and shown in Fig. 5. Upper limits were derived by eye. They are stated as best-fit values, with an uncertainty that indicates at which abundance the predicted lines become clearly too strong. The analysis of individual metal abundances is described in the following.

Plenty of strong C II-IV, N II-III, and O II-III lines are present in the spectrum of EC 22536–5304 A. The C II atom was updated to use resonance-averaged photo-ionisation cross-sections using data from TOPbase ([Cunto et al. 1993](#)). This slightly changes the strengths of C II lines, but it has little effect on the general atmospheric structure because C II represents a small fraction of all carbon ions throughout the atmosphere ( $< 2\%$ ). The sdOB star is enriched in carbon and nitrogen and has an approximately solar oxygen abundance. The carbon, nitrogen, and oxygen lines in the spectrum of the F-type companion are too weak to be detected. The Mg II 4481 Å doublet is present in both components, but the contribution of the sdOB is larger, despite its sub-solar magnesium abundance. This is because the flux contribution of the sdOB star is more than twice that of the F-type companion in this specific range. The derived silicon abundance for the sdOB, about one-tenth solar, is mostly based on the strong Si IV 4088.9, 4116.1 Å lines and the weaker Si III 4552.6 Å line. The only detected silicon line that originates from the cool companion, Si I 3905.52 Å, is consistent with an alpha-enhancement of 0.4 dex. Two weak phosphorus lines in the spectrum of the sdOB, P III 4222.2 Å and P IV 4249.7 Å, are clearly identified. They are best reproduced at an abundance of about five times solar. All detected calcium lines originate from the cool component. Most notably, the Ca I 4226.7 Å resonance line and the Ca II 8498, 8542, 8662 Å triplet are well reproduced at an alpha-enhancement of 0.4 dex.

As shown in Fig. 6, strong Pb IV lines are present at rest wavelengths of 3962.5, 4049.8, 4174.5, 4496.2, 4534.4, 4534.9, and 4605.4 Å. Although weaker, Pb III lines at 3854.1, 4272.7, 4571.2, 4761.1, and 4798.6 Å are clearly detected. All identified lead lines are listed in Table 5. The 2019 HRS spectra were shifted to the rest frame of the sdOB and co-added to update the wavelengths of newly observed lead lines. This co-added spec-

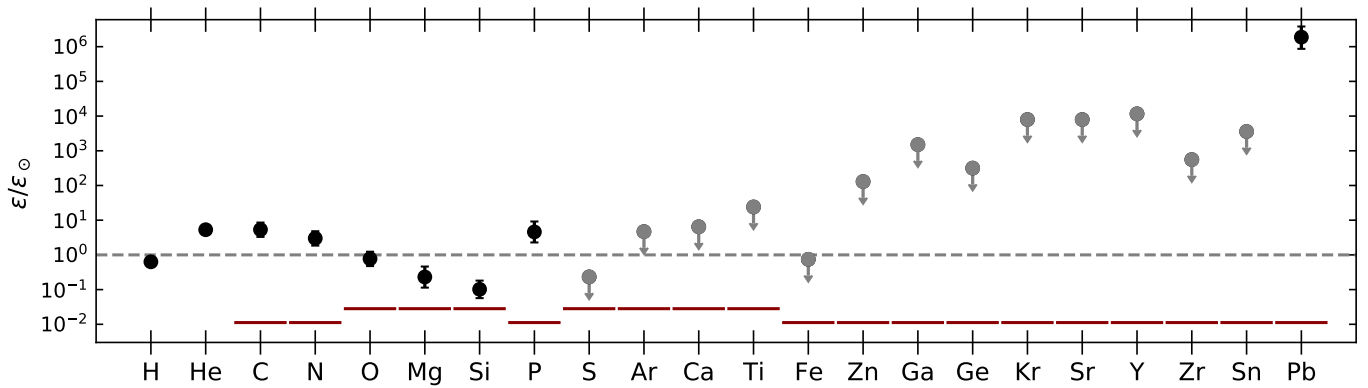


Fig. 5: Photospheric abundances for EC 22536–5304 A relative to solar values from [Asplund et al. \(2009\)](#). Abundance measurements are shown as black dots, while upper limits are marked with grey arrows. Solid red lines show the corresponding metal abundances adopted in our model for EC 22536–5304 B, as given by the best-fit  $[\text{Fe}/\text{H}]$  and  $[\alpha/\text{Fe}]$ . The solar reference is indicated by the dashed grey line.

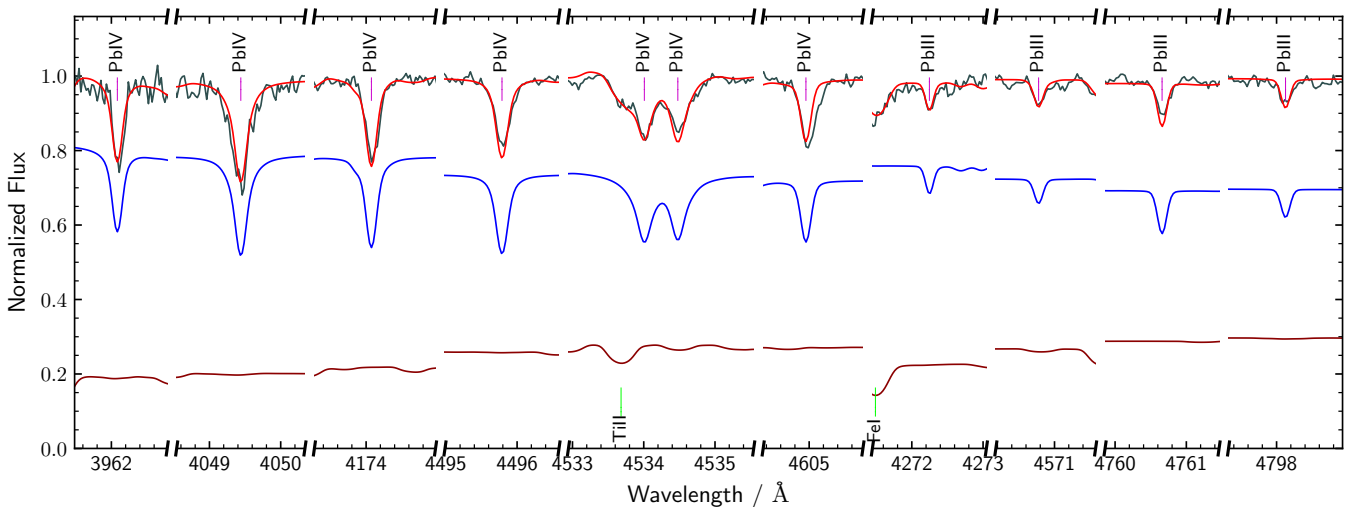


Fig. 6: Very strong lead lines in the HRS spectrum of EC 22536–5304 (grey). The combined model spectrum (red) is the sum of the contributions of the sdOB (blue) and F-type star (dark red).

trum was not used for the abundance fit, which, as before, was performed using all individual spectra. All modelled lead lines are reasonably well reproduced at an abundance between one and two million times solar, or 100 million times larger than the scaled solar value using the metallicity deduced from the cool companion. This is significantly more than the 4.8 dex enrichment derived by [Jeffery & Miszalski \(2019\)](#), who were unaware of any flux contribution from a companion.

Table 4 also lists upper limits for several elements, which had been detected in other iHe sdOBs, in particular Feige 46 and LS IV–14°116 ([Dorsch et al. 2020](#)). Since no lines from these elements are detected, any ‘best-fit’ abundance obtained from a  $\chi^2$  fit would strongly depend on the location of the continuum. We therefore prefer to obtain upper limits by eye. All lines used to derive upper limits for EC 22536–5304 A up to iron are known to be well reproduced in our models of other He-sdOB stars. For sulphur, we used the weak S IV 4485.7, 4504.2 Å lines, which seem to be just below the detection limit of the HRS and UVES spectra of EC 22536–5304. The only usable predicted argon line is Ar III 4183.0 Å. The upper limits for calcium and titanium are based on Ca III 4233.7, 4240.7 Å, and Ti IV 4618.2,

5398.9, 5492.5 Å, respectively. The upper limit for iron is based on the non-detection of Fe III 4164.7, 4304.8, and 4310.4 Å. In addition to lead, we also searched for heavy metals that have been detected in optical spectra of the intermediate He-sdOBs Feige 46 and LS IV–14°116: Zn, Ga, Ge, Kr, Sr, Y, Zr, and Sn. Upper limits for these elements are based on the non-detection of Zn III 4818.9, 5075.2 Å, Ga III 4380.6, 4381.8, 4993.9 Å, Ge III 4179.1, 4260.9 Å, Kr III 4067.4, 4226.6 Å, Sr III 3936.4 Å, Y III 4039.6, 4040.1 Å, Zr IV 4198.3, 5462.4 Å, and Sn IV 4216.2 Å. We used the same atomic data as [Dorsch et al. \(2020\)](#) for these ions. The resulting upper limits rule out extreme enrichments as observed for lead, but would still be consistent with strong enrichment compared to solar or even mean sdB values. Ultraviolet spectra would enable us to determine abundances for most of these heavy metals, but they are not presently available. A small number of lines in the UVES and HRS spectra remain unidentified. The identification of these lines is complicated by the composite nature of EC 22536–5304, since the lines of the F-type companion are only slightly more broadened by rotation than those of the sdOB. Table A.2 lists the rest wavelengths of all detected unidentified lines, assuming that they originate from

the sdOB component. We only list lines that are present in both coadded HRS and coadded UVES spectra, or are strong enough to be identified in single exposures.

The overall abundance pattern for EC 22536–5304 A is similar to that derived by Jeffery & Miszalski (2019), but shifted to higher abundances due to the contribution of the sdF star (unaccounted for previously). Carbon, nitrogen, and phosphorus are enhanced relative to solar values, while the oxygen abundance is about solar. Magnesium, silicon, and sulphur are sub-solar. With respect to the primordial metallicity plus alpha enhancement, all detected elements would be enhanced. Similar patterns for these light metals have been observed in other heavy-metal iHe-sdOBs: the zirconium-rich Feige 46 and LS IV–14°116 (Naslim et al. 2011; Dorsch et al. 2020), the zirconium- and lead-rich HE 2359–2844 and HE 1256–2738 (Naslim et al. 2013), the lead-rich PG 1559+048 and FBS 1749+373 (Naslim et al. 2020), as well as PG 0909+276 and UVO 0512–08 (Edelmann et al. 2003; Wild & Jeffery 2018), which are extremely enriched in iron-group elements. Unlike the hotter lead-rich iHe-sdOBs UVO 0825+15 (Jeffery et al. 2017), HZ 44, and HD 127493 (Dorsch et al. 2019), EC 22536–5304 A does not show the distinct CNO-cycle pattern (strong N, weak C and O). Notably, the metal abundance pattern is not shifted to lower values when compared to other heavy-metal iHe-sdOBs. This indicates that the metal abundance patterns observed for iHe-sdOB stars are not strongly dependent on the initial metallicity. The abundances derived for C, N, O, and Si are almost identical to those of HE 1256–2738, an apparently single lead-rich iHe-sdOB found to be a Galactic halo member by Martin et al. (2017).

EC 22536–5304 A does not seem to share the extreme zirconium abundance observed in some iHe-sdOBs or the extreme enrichment in iron-group elements with respect to the Sun found in others, although our upper limits are high. The latter may be due to the very low primordial metallicity of the system. The lead enhancement of EC 22536–5304 A is the most extreme found in any hot subdwarf, or, to our knowledge, in any star. The strong enrichment of heavy metals in the photospheres of heavy-metal sdOBs is usually discussed in terms of selective radiative levitation. In this picture, the strong heavy metal lines observed in the emergent spectrum are the result of a chemically stratified envelope, in which a thin metal-rich layer overlaps with the line-forming region. As mentioned by Jeffery & Miszalski (2019), atmospheric models that include a physical treatment of stratification by diffusion are required to estimate the total amount of lead in the enriched layers. These models would then have to be compared with lines that form at various optical depths, ideally using both far-UV and optical spectra.

The flux contribution of the sdF only overtakes that of the sdOB at about 7200 Å in our best-fit model. Therefore, and due to the low metallicity, relatively few metal lines that originate from the sdF component are detectable in our spectra. Most of them are well reproduced at the best-fit metallicity and alpha-enhancement. The strongest metal lines detected include transitions in the Na I, Mg I, Al I, Si I, Ca I–II, Ti II, Cr I, Mn I, Fe I–II, and Ni I atoms. The strontium lines Sr II 4077.7, 4215.5 Å seem to be well reproduced at the scaled solar abundance. We also detect Ba II 4554.0, 4934.1 Å, which are somewhat too weak in our models at the scaled solar abundance. This discrepancy may be due to a weak enrichment in barium, but may also be caused by deficiencies in our synthetic spectra, such as uncertain atomic data or NLTE effects. The existence of dwarf barium stars is usually explained with pollution through wind accretion or RLOF from an AGB star (Jorissen & Boffin 1992; Gray et al.

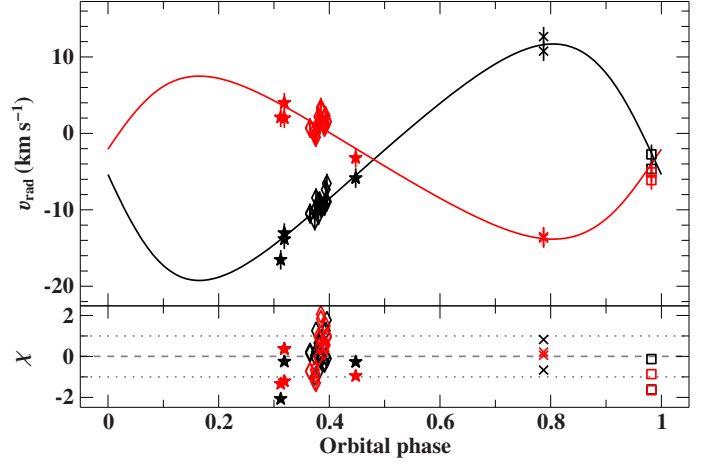


Fig. 7: Elliptic orbits fit to the radial velocities of both EC 22536–5304 A (black) and B (red). Asterisks indicate UVES measurements, while HRS data from 2017, 2018, and 2019 are marked by crosses, squares, and diamonds, respectively.

Table 6: Orbital parameters for EC 22536–5304. The gravitational redshift  $v_{\text{grav}}$  is calculated from the stellar parameters listed in Table 3.

Parameter	Value
Period $P$	$457.0^{+1.2}_{-1.5}$ d
Epoch of periastron $T_{\text{periastron}}$	$56160^{+21}_{-17}$ MJD
Eccentricity $e$	$0.22^{+0.13}_{-0.08}$
Longitude of periastron $\omega$	$276^{+21}_{-18}$ deg
Velocity semiamplitude $K_A$	$15.5^{+1.7}_{-1.6}$ km s $^{-1}$
Velocity semiamplitude $K_B$	$10.7 \pm 1.4$ km s $^{-1}$
Gravitational redshift $v_{\text{grav}A}$	$1.95^{+0.22}_{-0.20}$ km s $^{-1}$
Gravitational redshift $v_{\text{grav}B}$	$0.72^{+0.21}_{-0.17}$ km s $^{-1}$
Systemic velocity $\gamma$	$-3.3 \pm 0.4$ km s $^{-1}$
Derived parameter	Value
Mass ratio $q = K_B/K_A = M_A/M_B$	$0.69^{+0.06}_{-0.05}$
Projected semimajor axis $a_A \sin(i)$	$0.63 \pm 0.05$ au
Projected semimajor axis $a_B \sin(i)$	$0.44 \pm 0.04$ au

2011). Given that EC 22536–5304 A is likely still on the horizontal branch, it seems unlikely that the sdF component is a barium star.

It is likely that the present EC 22536–5304 system formed through mass transfer from a RGB star to the sdF companion. One might therefore expect at least some pollution of the sdF companion by material processed in the CNO-cycle, although diluted by convection. Unfortunately, no carbon, nitrogen, or oxygen lines that originate from the sdF are detectable in our spectra.

## 7. Analysis of the radial velocity curve

A total of 27 HRS and UVES spectra are of sufficient quality to measure the radial velocities for both components, which are listed in Table A.3. These spectra cover a time span of  $\Delta t = 2880$  days, but they were taken in only five observing runs, the longest of which was just two weeks. This coverage



is too irregular to precisely determine the orbital parameters of the EC 22536–5304 system. We initially searched for orbital periods by fitting circular orbits to all available radial velocities, corrected for the gravitational redshifts. A unique best orbital period,  $P \approx 457$  days, was obtained by finely sampling orbital frequencies between  $1/330$  and  $1/550 \text{ d}^{-1}$  with steps of  $0.01/\Delta t = 3.6 \times 10^{-6} \text{ d}^{-1}$ . Fitting eccentric orbits resulted in a somewhat eccentric orbit with the same 457-day period and velocity semi-amplitudes of  $K_A = 15.5 \pm 1.7 \text{ km s}^{-1}$  and  $K_B = 10.7 \pm 1.4 \text{ km s}^{-1}$  (see Table 6). The phased radial velocity curves are shown in Fig. 7. More observations are required to improve the orbital solution, in particular for the eccentricity.

Since the orbital period of EC 22536–5304 is certainly longer than 50 days, it is likely that the system was formed through stable Roche-lobe overflow. Vos et al. (2017) discovered a positive correlation between the eccentricity and orbital period for post-RLOF systems. Given the orbital period of about 457 days, one would expect a low eccentricity for the orbit of EC 22536–5304. We find an eccentricity of  $e = 0.22^{+0.13}_{-0.08}$ , which, however, strongly depends on the radial velocities derived from the HRS spectra taken in 2017.

A correlation between orbital period and mass ratio of post-RLOF sdB+MS binaries was found by Vos et al. (2019). Subsequently, Vos et al. (2020) showed that the observed relation can be explained in terms of the system metallicity. Orbital periods of sdB+MS systems decrease with metallicity, because low-metallicity donor stars have smaller radii at the top of the RGB. In order to produce a sdB, the mass transfer must happen close to the top of the RGB, so that the RGB star can ignite helium burning in its core. Low-metallicity systems therefore have shorter initial periods, which leads to shorter final periods once the mass transfer has stopped. For halo systems at  $[\text{Fe}/\text{H}] = -1.8 \pm 0.5$ , Vos et al. (2020) predicted orbital periods of 300 to 500 days and mass ratios  $q = M_{\text{sdb}}/M_{\text{MS}}$  of 0.6 to 0.8, which is consistent with our (preliminary) result for EC 22536–5304,  $q = K_B/K_A = M_A/M_B = 0.69 \pm 0.06$ . Assuming a canonical mass of  $M_{\text{sdb}} = 0.49 M_{\odot}$  for the sdOB, the mass ratio would put the mass of the sdF at  $0.71 \pm 0.06 M_{\odot}$ .

## 8. Kinematics

Proper motions and the parallax from *Gaia* EDR3 combined with the system’s radial velocity can be used to derive the present 3D space velocity of EC 22536–5304. The Galactic orbit of EC 22536–5304 can then be traced back using a model for the Galactic potential: here, for 10 Gyr. We used Model I of Irigang et al. (2013) for the Galactic potential, which is a revision of the Allen & Santillan (1991) potential. Given the sparse coverage of our radial velocities, we adopted an uncertainty of  $5 \text{ km s}^{-1}$  on the system’s radial velocity. The resulting orbit for EC 22536–5304 has a low angular momentum perpendicular to the Galactic disc  $J_Z = 930 \pm 40 \text{ kpc km s}^{-1}$ , but a relatively high eccentricity of  $e = 0.53 \pm 0.02$ . The current velocity towards the Galactic centre  $U$ , perpendicular to the disc  $W$ , and in the direction of Galactic rotation  $V$  can be used to place EC 22536–5304 in the Toomre diagram. When compared to the Toomre parameters predicted from Besançon Galactic models (Robin et al. 2003), the location of EC 22536–5304 in this diagram is consistent with either a thick-disc or halo origin (see Fig. 8). Although most hot subdwarf stars seem to be part of the thin disc, several intermediate He-sdO/Bs in the sample of Martin et al. (2017) have been classified as thick discs or halos. To facilitate the comparison with EC 22536–5304, we repeated the orbit calculation for iHe-sdOBs from this sample using reliable

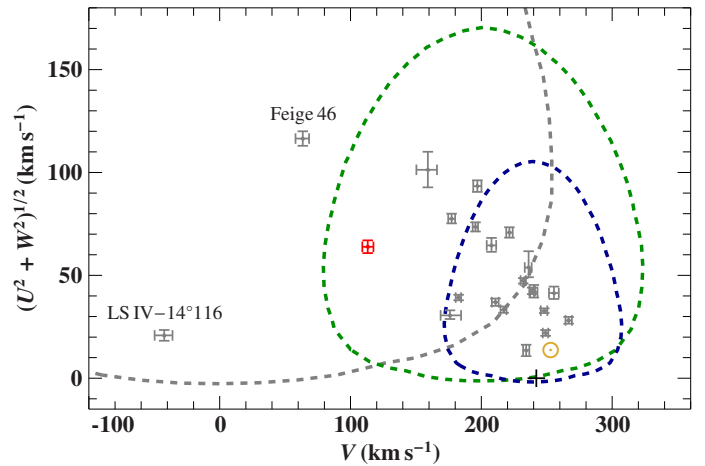


Fig. 8: Toomre diagram showing space velocities with respect to the Galactic centre. The velocity component  $V$  is measured in the direction of the rotation of the Galaxy,  $U$  towards the Galactic centre, and  $W$  perpendicular to the plane. The position of EC 22536–5304, the Sun, and the local standard of rest (LSR) are marked by the red cross, yellow circled dot, and black plus sign, respectively. The grey, green, and blue dashed lines indicate  $2\text{-}\sigma$  velocity dispersions from Robin et al. (2003) for the halo, thick disc, and old thin disc, respectively. Stars from the sample of intermediate He-sdO/Bs studied by Martin et al. (2017), updated using *Gaia* EDR3 parallaxes and proper motions are shown in grey. Probable halo stars are labelled.

*Gaia* EDR3 proper motions and parallaxes ( $\sigma_{\varpi}/\varpi < 10\%$ ). The heavy-metal iHe-sdOBs Feige 46 and HZ 44 (Dorsch et al. 2019, 2020) were considered in addition. We corrected the proper motions provided by *Gaia* EDR3 for bright stars ( $G < 13 \text{ mag}$ ), following Cantat-Gaudin & Brandt (2021). As before, we applied corrections to the parallax measurements (Lindgren et al. 2021) and their uncertainty (El-Badry et al. 2021). The resulting orbital parameters are summarised in Table A.4.

Given the low metallicity of EC 22536–5304, the system may be part of the low-metallicity tail of the thick disc, also termed metal-weak thick disc (MWTD). According to Chiba & Beers (2000), the low-metallicity cut-off of the MWTD is close to  $[\text{Fe}/\text{H}] = -2$ , comparable to the metallicity of EC 22536–5304 B. At this low metallicity, the halo population in their sample dominates even at small distances from the Galactic disc, such as the  $Z = -593^{+13}_{-16} \text{ pc}$  observed for EC 22536–5304. However, is not possible to discern between a MWTD or halo origin for any particular system that shows disc-like kinematics (see e.g. Reddy & Lambert 2008).

## 9. Conclusions

We performed a detailed analysis of high-resolution spectra of EC 22536–5304 and can confirm that the system contains an extremely lead-rich intermediate He-sdOB, as found by Jeffery & Miszalski (2019). However, we find a second component in its spectrum: a strongly alpha-enhanced and metal-poor F-type subdwarf. EC 22536–5304 A is the first heavy-metal sdOB found in a binary system. Our updated metal abundances for the sdOB component are similar to those derived in the previous analysis, but shifted to higher abundances. EC 22536–5304 A therefore remains the most lead-rich hot subdwarf known to date. Although the initial metallicity of the system is low, the abun-

dances for the hot component are quite similar to those of other iHe-sdOB stars, some of which probably have significantly higher initial metallicities, given that they belong to the younger thin-disc population (such as PG 1559+048, see Sect. 8). The observed abundance pattern of EC 22536–5304 A is likely the result of strong diffusion processes. Ultraviolet spectroscopy would enable us to derive a more complete abundance pattern for the sdOB component.

EC 22536–5304 A is the first hot subdwarf found in a long-period binary with a known metallicity  $[\text{Fe}/\text{H}] < -1$ . The low metallicity ( $[\text{Fe}/\text{H}]_{\text{B}} = -1.95$ ) and strong  $\alpha$  enhancement ( $[\alpha/\text{Fe}]_{\text{B}} = 0.4$ ) derived for the sdF component indicate that the system is part of the Galactic halo or metal-weak thick disc. The system is therefore likely old ( $\geq 10$  Gyr, e.g. Helmi 2020). Other hot subdwarfs with a low known metallicity are part of globular clusters, but they are typically not found in binary systems (Latour et al. 2018). Still, the stellar evolution models of Han (2008) predict a significant fraction of old sdOBs to have been formed through stable RLOF, which seems to be the case for EC 22536–5304.

To determine the stellar parameters mass, radius, and luminosity for both components, we combined the parallax provided by *Gaia* EDR3 with the angular diameter derived from a SED fit and our spectroscopic atmospheric parameters. The resulting mass for EC 22536–5304 A,  $0.40 \pm 0.06 M_{\odot}$ , is consistent with the range of masses expected for hot subdwarf stars on the extreme horizontal branch. The spectroscopic mass for EC 22536–5304 B,  $0.84^{+0.29}_{-0.23} M_{\odot}$ , is associated with a high uncertainty because its surface gravity is not easily determined. In fact, the comparison of MIST evolutionary tracks with our effective temperature and luminosity points to a lower mass for the sdF, about  $0.7 M_{\odot}$ . This mass would be consistent with an evolutionary age of about 10 Gyr.

Radial velocity variations suggest that the system is likely a wide binary with an orbital period of about 457 days. An eccentric fit to the radial velocities results in a mass ratio  $q = M_A/M_B = 0.69 \pm 0.06$ . Vos et al. (2019) recently found a strong relation between the orbital period and mass ratio for long-period hot subdwarf binaries. This relation could be explained by a correlation between the final orbital period and metallicity of such systems found by Vos et al. (2020), which results from different radii of the progenitors at the tip of the RGB, when mass transfer started. Given the low metallicity of EC 22536–5304, the system helps to constrain these relations at much lower metallicity than before. The current results for the orbital period, mass ratio, and metallicity are consistent with the predictions of Vos et al. (2020) for post-RLOF systems. Additional spectra that sample the full orbital period are required to obtain reliable orbital parameters.

We also performed a kinematic analysis, based on the system radial velocity determined from the current radial velocity curve. EC 22536–5304 is on an eccentric orbit around the Galactic centre, which is consistent with a halo or thick-disc membership. Several heavy-metal iHe-sdOB stars have been found in the Galactic halo. From the *Gaia* EDR3 data, we can confirm that the zirconium-rich Feige 46 and LS IV–14° 116 (Latour et al. 2019b; Dorsch et al. 2020) are halo members.

**Acknowledgements.** We thank the referee for the careful reading and comments that improved this paper. A.L., U.H. and M.D. acknowledge funding by the Deutsche Forschungsgemeinschaft (DFG) through grants IR190/1-1, HE1356/70-1 and HE1356/71-1. This research made use of the *lmfit* python package developed by Newville et al. (2014). Based on observations obtained with the Southern African Large Telescope (SALT) under programmes 2017-1-SCI-004, 2018-2-SCI-033, and 2019-1-MLT-003. Based on observations collected at the European Southern Observatory under ESO programme 088.D-0364(A). This work has made use of data from the European Space Agency

(ESA) mission *Gaia* (<https://www.cosmos.esa.int/gaia>), processed by the *Gaia* Data Processing and Analysis Consortium (DPAC, <https://www.cosmos.esa.int/web/gaia/dpac/consortium>). Funding for the DPAC has been provided by national institutions, in particular the institutions participating in the *Gaia* Multilateral Agreement. This publication makes use of data products from the Wide-field Infrared Survey Explorer, which is a joint project of the University of California, Los Angeles, and the Jet Propulsion Laboratory/California Institute of Technology, funded by the National Aeronautics and Space Administration. This research has made use of NASA's Astrophysics Data System. The Armagh Observatory and Planetarium are funded by direct grant from the Northern Ireland Department for Communities.

## References

- Abbott, T. M. C., Abdalla, F. B., Allam, S., et al. 2018, *ApJS*, 239, 18  
 Ahmad, A. & Jeffery, C. S. 2005, *A&A*, 437, L51  
 Allen, C. & Santillan, A. 1991, *Rev. Mexicana Astron. Astrofis.*, 22, 255  
 Alonso-Medina, A., Colón, C., & Porcher, P. 2011, *Atomic Data and Nuclear Data Tables*, 97, 36  
 Alonso-Medina, A., Colón, C., & Zanón, A. 2009, *MNRAS*, 395, 567  
 Asplund, M., Grevesse, N., Sauval, A. J., & Scott, P. 2009, *ARA&A*, 47, 481  
 Bailer-Jones, C. A. L., Rybizki, J., Fournesneau, M., Mantelet, G., & Andrae, R. 2018, *AJ*, 156, 58  
 Cantat-Gaudin, T. & Brandt, T. D. 2021, *A&A*, 649, A124  
 Chen, X., Han, Z., Deca, J., & Podsiadlowski, P. 2013, *MNRAS*, 434, 186  
 Chiba, M. & Beers, T. C. 2000, *AJ*, 119, 2843  
 Choi, J., Dotter, A., Conroy, C., et al. 2016, *ApJ*, 823, 102  
 Cunto, W., Mendoza, C., Ochsenbein, F., & Zeippen, C. J. 1993, *A&A*, 275, L5  
 Cutri, R. M., Skrutskie, M. F., van Dyk, S., et al. 2003, *VizieR Online Data Catalog*, 2246  
 Cutri, R. M., Wright, E. L., Conrow, T., et al. 2021, *VizieR Online Data Catalog*, II/328  
 DENIS Consortium. 2005, *VizieR Online Data Catalog: The DENIS database*  
 Dorman, B., Rood, R. T., & O'Connell, R. W. 1993, *ApJ*, 419, 596  
 Dorsch, M., Latour, M., & Heber, U. 2019, *A&A*, 630, A130  
 Dorsch, M., Latour, M., Heber, U., et al. 2020, *A&A*, 643, A22  
 Edelmann, H., Heber, U., Hagen, H. J., et al. 2003, *A&A*, 400, 939  
 El-Badry, K., Rix, H.-W., & Heintz, T. M. 2021, *MNRAS*[arXiv:2101.05282]  
 Fitzpatrick, E. L., Massa, D., Gordon, K. D., Bohlin, R., & Clayton, G. C. 2019, *ApJ*, 886, 108  
 Fuhrmann, K. 1998, *A&A*, 338, 161  
 Gaia Collaboration, Brown, A. G. A., Vallenari, A., et al. 2021, *A&A*, 649, A1  
 Gaia Collaboration, Prusti, T., de Bruijne, J. H. J., et al. 2016, *A&A*, 595, A1  
 Geier, S. & Heber, U. 2012, *A&A*, 543, A149  
 Goy, G. 1980, *A&A*, 88, 370  
 Gray, R. O., McGahee, C. E., Griffin, R. E. M., & Corbally, C. J. 2011, *AJ*, 141, 160  
 Han, Z. 2008, *A&A*, 484, L31  
 Han, Z., Podsiadlowski, P., Maxted, P. F. L., & Marsh, T. R. 2003, *MNRAS*, 341, 669  
 Han, Z., Podsiadlowski, P., Maxted, P. F. L., Marsh, T. R., & Ivanova, N. 2002, *Monthly Notices of the Royal Astronomical Society*, 336, 449  
 Heber, U. 2009, *Annual Review of Astronomy and Astrophysics*, 47, 211  
 Heber, U. 2016, *Publications of the Astronomical Society of the Pacific*, 128, 082001  
 Heber, U., Irrgang, A., & Schaffenroth, J. 2018, *Open Astronomy*, 27, 35  
 Helmi, A. 2020, *ARA&A*, 58, 205  
 Henden, A. A., Levine, S., Terrell, D., & Welch, D. L. 2015, in *American Astronomical Society Meeting Abstracts*, Vol. 225, American Astronomical Society Meeting Abstracts #225, 336.16  
 Høg, E., Fabricius, C., Makarov, V. V., et al. 2000, *A&A*, 355, L27  
 Hu, H., Tout, C. A., Glebbeek, E., & Dupret, M. A. 2011, *MNRAS*, 418, 195  
 Hubeny, I. & Lanz, T. 2017a, *ArXiv e-prints* [arXiv:1706.01859]  
 Hubeny, I. & Lanz, T. 2017b, *ArXiv e-prints* [arXiv:1706.01935]  
 Hubeny, I. & Lanz, T. 2017c, *ArXiv e-prints* [arXiv:1706.01937]  
 Irrgang, A., Geier, S., Kreuzer, S., Pelisoli, I., & Heber, U. 2020, *A&A*, 633, L5  
 Irrgang, A., Przybilla, N., Heber, U., et al. 2014, *A&A*, 565, A63  
 Irrgang, A., Wilcox, B., Tucker, E., & Schiefelbein, L. 2013, *A&A*, 549, A137  
 Jeffery, C. S., Baran, A. S., Behara, N. T., et al. 2017, *MNRAS*, 465, 3101  
 Jeffery, C. S. & Miszalski, B. 2019, *MNRAS*, 489, 1481  
 Jeffery, C. S., Miszalski, B., & Snowden, E. 2021, *MNRAS*, 501, 623  
 Jorissen, A. & Boffin, H. M. J. 1992, in *Binaries as Tracers of Star Formation*, 110–131  
 Kilkenny, D., Worters, H. L., O'Donoghue, D., et al. 2016, *MNRAS*, 459, 4343  
 Kupfer, T., Geier, S., Heber, U., et al. 2015, *A&A*, 576, A44  
 Kurucz, R. L. 1993, *SYNTHES spectrum synthesis programs and line data*

- Kurucz, R. L. 1996, in *Astronomical Society of the Pacific Conference Series*, Vol. 108, M.A.S.S., *Model Atmospheres and Spectrum Synthesis*, ed. S. J. Adelman, F. Kupka, & W. W. Weiss, 160
- Lanz, T. & Hubeny, I. 2003, *ApJS*, 146, 417
- Latour, M., Dorsch, M., & Heber, U. 2019a, *A&A*, 629, A148
- Latour, M., Green, E. M., & Fontaine, G. 2019b, *A&A*, 623, L12
- Latour, M., Randall, S. K., Calamida, A., Geier, S., & Moehler, S. 2018, *A&A*, 618, A15
- Lindgren, L., Bastian, U., Biermann, M., et al. 2021, *A&A*, 649, A4
- Martin, P., Jeffery, C. S., Naslim, N., & Woolf, V. M. 2017, *MNRAS*, 467, 68
- McMahon, R. G., Banerji, M., Gonzalez, E., et al. 2013, *The Messenger*, 154, 35
- Michaud, G., Richer, J., & Richard, O. 2011, *A&A*, 529, A60
- Moehler, S., Modigliani, A., Freudling, W., et al. 2014, *A&A*, 568, A9
- Naslim, N., Jeffery, C. S., Behara, N. T., & Hibbert, A. 2011, *MNRAS*, 412, 363
- Naslim, N., Jeffery, C. S., Hibbert, A., & Behara, N. T. 2013, *MNRAS*, 434, 1920
- Naslim, N., Jeffery, C. S., & Woolf, V. M. 2020, *MNRAS*, 491, 874
- Németh, P., Kawka, A., & Vennes, S. 2012, *MNRAS*, 427, 2180
- Németh, P., Vos, J., Molina, F., & Bastian, A. 2021, *arXiv e-prints*, arXiv:2107.03270
- Newville, M., Stensitzki, T., Allen, D. B., & Ingargiola, A. 2014, *LMFIT: Non-Linear Least-Square Minimization and Curve-Fitting for Python*
- Orlov, V. G., Voitsekhovich, V. V., Rivera, J. L., Guerrero, C. A., & Ortiz, F. 2010, *Rev. Mexicana Astron. Astrofis.*, 46, 245
- Østensen, R. H., Jeffery, C. S., Saio, H., et al. 2020, *MNRAS*, 499, 3738
- Rauch, T. 1993, *A&A*, 276, 171
- Reddy, B. E. & Lambert, D. L. 2008, *MNRAS*, 391, 95
- Riello, M., De Angeli, F., Evans, D. W., et al. 2021, *A&A*, 649, A3
- Robin, A. C., Reylé, C., Derrière, S., & Picaud, S. 2003, *A&A*, 409, 523
- Safronova, U. I. & Johnson, W. R. 2004, *Phys. Rev. A*, 69, 052511
- Schaffenroth, V., Casewell, S. L., Schneider, D., et al. 2021, *MNRAS*, 501, 3847
- Schlegel, D. J., Finkbeiner, D. P., & Davis, M. 1998, *ApJ*, 500, 525
- Tomley, L. 1970, *ApJ*, 162, 239
- Vos, J., Bobrick, A., & Vučković, M. 2020, *A&A*, 641, A163
- Vos, J., Németh, P., Vučković, M., Østensen, R., & Parsons, S. 2018, *MNRAS*, 473, 693
- Vos, J., Østensen, R. H., Vučković, M., & Van Winckel, H. 2017, *A&A*, 605, A109
- Vos, J., Vučković, M., Chen, X., et al. 2019, *MNRAS*, 482, 4592
- Wild, J. F. & Jeffery, C. S. 2018, *MNRAS*, 473, 4021
- Wolf, C., Onken, C. A., Luvaul, L. C., et al. 2018, *PASA*, 35, e010

Table A.1: Dimensions for the four grids of synthetic spectra used for the spectroscopic and SED analyses. For each parameter, the maximum and minimum values, as well as the step width are stated. As described in Sect. 4, the large and small TLUSTY/SYNPEC grids were each computed using a fixed metal abundance pattern.

Parameter	TLUSTY/SYNPEC		ATLAS12/SYNTH	
	large	small	large	small
$T_{\text{eff}}$ (K)	27500	37300	4000	6150
	47500	38800	8000	6275
	1250	500	200	25
$\log g$	4.750	5.60	2.00	4.50
	6.125	6.00	5.20	4.80
	0.125	0.20	0.20	0.10
$\log n(\text{He})/n(\text{H})$	-1.00	-0.23	-1.07	-1.07
	+2.00	+0.07	-1.07	-1.07
	0.25	0.15	-	-
[Fe/H]	-	-	-2.00	-2.05
	-	-	+0.50	-1.85
	-	-	0.50	0.20
[ $\alpha$ /Fe]	-	-	0.40	0.33
	-	-	0.40	0.44
	-	-	-	0.11
$v_{\text{tb}}$ (km s <sup>-1</sup> )	5.0	0.0	0.0	1.5
	5.0	3.0	2.0	2.5
	-	3.0	1.0	1.0

Table A.2: Unidentified lines in the HRS and UVES spectra of EC 22536–5304. Equivalent widths are stated for the composite spectrum. Rest wavelengths assume that lines originate from the sdOB.

$\lambda$ / Å	EW / mÅ	Comment
4081.692	19	sharp
4182.414	11	sharp
4273.738	12	
4400.840	10	
4450.986	8	
4581.979	25	broad
4664.656	13	broad
4802.251	12	
5021.613	27	artifact?
5094.107	15	
5438.381	22	
7298.346	78	

Table A.3: Radial velocities with barycentric correction applied. The gravitational redshifts have not been corrected. The typical uncertainty is of the order of 2 km s<sup>-1</sup>, depending on S/N. There may be a small systematic trend in the radial velocities derived from HRS spectra that were taken in 2019.

MJD	$v_{\text{rad,B}}$ / km s <sup>-1</sup>	$v_{\text{rad,A}}$ / km s <sup>-1</sup>	Spectrograph
55846.1	4.0	-14.6	UVES
55846.1	4.1	-15.7	UVES
55849.1	6.0	-12.2	UVES
55849.1	4.0	-13.0	UVES
55908.0	-1.2	-5.0	UVES
57891.0	-11.7	13.5	HRS
57891.0	-11.5	11.6	HRS
58437.0	-3.3	-3.2	HRS
58437.0	-4.2	-0.3	HRS
58612.0	2.4	-10.5	HRS
58612.0	2.6	-9.4	HRS
58616.0	1.9	-10.7	HRS
58616.0	2.1	-11.0	HRS
58617.0	2.0	-8.3	HRS
58617.0	2.3	-8.8	HRS
58619.0	4.1	-10.0	HRS
58619.0	2.9	-7.5	HRS
58620.0	2.5	-7.6	HRS
58620.0	4.9	-8.0	HRS
58621.0	3.9	-8.4	HRS
58621.0	3.8	-9.0	HRS
58624.0	3.4	-8.4	HRS
58624.0	3.0	-7.4	HRS
58625.0	3.4	-7.4	HRS
58625.0	4.1	-7.3	HRS
58626.0	3.3	-7.9	HRS
58626.0	4.1	-7.2	HRS

spectra. We show the co-added 2019 HRS spectra and two examples for the UVES spectra. The 2019 HRS spectra were shifted to a common radial velocity for the sdOB component before they were co-added. Lines that originate from the sdF component are therefore very slightly broadened in this spectrum. The observations were normalised to match the continuum levels of our synthetic spectra. Telluric lines in the red spectra were removed using the grid of transmission spectra provided by [Moehler et al. \(2014\)](#). The strongest metal lines for the sdOB are labelled on top, while lines of the sdF are labelled at the bottom. The combined model is shown in red, while the contributions of the sdOB and sdF components are shown in blue and dark red, respectively.

## Appendix A: Additional material

### Appendix B: Full spectral comparisons

This section presents the full spectral comparison between the observed spectra of EC 22536–5304 and our final synthetic



Table A.4: Orbital parameters for a sample of intermediate He sdOB stars studied by (Martin et al. 2017) and recent additions (HZ 44, Feige 46, EC 22536–5304). The quantities  $R_{\max}$ ,  $R_{\min}$ , and  $Z_{\max}$  refer to the maximum and minimum distance from the Galactic centre, as well as the maximum distance from the Galactic disc. Known zirconium- or lead-rich stars are marked by  $^{\dagger}$ .

Star	$v_{\text{rad}}$ km s <sup>-1</sup>	$\pm$	$R_{\max}$ kpc	$\pm$	$R_{\min}$ kpc	$\pm$	$Z_{\max}$ kpc	$\pm$	$V$ km s <sup>-1</sup>	$\pm$	$U$ km s <sup>-1</sup>	$\pm$	$W$ km s <sup>-1</sup>	$\pm$	$M_{\text{pc}}$ km s <sup>-1</sup>	$J_Z$ km s <sup>-1</sup>	$\pm$	$e$	$\pm$
PG 0909+276	20.0	2.0	9.23	0.18	8.59	0.05	0.42	0.03	249.1	2.1	-0.3	1.9	22.0	1.5		2.19	0.02	0.04	0.01
HD 127493 <sup>†</sup>	-17.0	3.0	8.42	0.08	7.60	0.13	0.10	0.01	234.2	2.4	13.3	2.5	-3.2	1.8		1.98	0.02	0.05	0.01
UVO 0512–08	11.0	3.3	9.46	0.20	8.24	0.07	0.44	0.03	248.1	2.5	-21.0	2.9	-25.2	1.6		2.17	0.03	0.07	0.02
HE 1238–1745	-7.9	2.8	9.18	0.15	7.19	0.12	0.96	0.07	240.2	2.8	39.1	3.1	15.6	2.1		1.97	0.03	0.12	0.01
PG 1559+048 <sup>†</sup>	-26.7	0.9	8.15	0.06	6.22	0.12	0.54	0.03	217.0	2.3	27.9	1.6	18.1	1.3		1.75	0.02	0.13	0.01
CPD –20 1123	-6.3	1.2	9.71	0.12	7.54	0.09	0.17	0.01	238.9	2.2	-41.4	1.5	8.4	0.7		2.10	0.02	0.13	0.01
SB 705	4.0	12.0	10.46	0.27	7.95	0.11	0.99	0.09	255.5	3.8	40.1	2.5	5.7	11.4		2.20	0.03	0.14	0.01
JL 87	-6.1	2.3	10.24	0.20	7.76	0.06	0.56	0.02	266.7	2.5	-27.6	1.9	5.7	1.5		2.17	0.02	0.14	0.01
UVO 0825+15 <sup>†</sup>	56.4	0.5	9.63	0.10	7.18	0.10	0.16	0.01	232.0	2.1	46.8	1.3	6.4	0.8		2.04	0.02	0.15	0.01
PG 0229+064	7.6	4.0	9.16	0.08	6.67	0.14	0.67	0.05	210.8	2.6	31.1	3.0	19.1	3.1		1.90	0.02	0.16	0.02
HE 2357–3940	-18.4	14.2	9.59	0.21	6.95	0.12	0.96	0.12	236.1	2.6	54.5	5.1	9.6	13.4		1.97	0.03	0.16	0.02
TON 414	2.7	0.5	10.08	0.12	6.75	0.16	1.44	0.13	207.8	3.6	-54.1	3.0	35.5	1.8		1.96	0.03	0.20	0.02
HE 1310–2733	41.5	1.9	9.12	0.09	5.95	0.12	0.94	0.05	221.4	2.4	-67.9	2.7	19.2	1.4		1.77	0.03	0.21	0.01
FBS 1749+373 <sup>†</sup>	-73.6	0.2	8.34	0.05	4.74	0.09	0.39	0.01	182.6	2.1	39.2	1.3	-2.5	0.8		1.51	0.02	0.28	0.01
HE 1136–2504	59.4	9.3	8.40	0.05	4.63	0.33	0.68	0.04	176.0	7.8	-30.4	1.6	5.6	5.5		1.48	0.07	0.29	0.04
TYC 3519-907-1	-62.7	0.2	9.30	0.08	5.12	0.09	0.30	0.01	195.5	2.1	73.5	2.2	2.7	0.9		1.66	0.02	0.29	0.01
PG 0240+046	63.4	2.0	10.57	0.11	5.36	0.13	0.57	0.03	196.9	3.1	93.4	2.8	0.6	2.1		1.78	0.03	0.33	0.02
HZ 44 <sup>†</sup>	-12.7	0.4	9.30	0.07	4.48	0.11	0.41	0.02	177.3	2.7	76.8	2.3	10.2	0.8		1.52	0.02	0.35	0.02
EC 22133–6446	-21.0	10.0	9.30	0.20	3.58	0.26	0.44	0.05	159.1	7.9	101.3	8.7	-2.9	7.2		1.31	0.07	0.44	0.04
EC 22536–5304 <sup>†</sup>	-3.3	5.0	8.21	0.05	2.51	0.13	1.50	0.12	113.2	4.2	-26.4	2.8	58.3	4.3		0.93	0.04	0.53	0.02
Feige 46 <sup>†</sup>	90.0	4.0	9.64	0.09	1.13	0.12	0.68	0.04	63.5	5.2	115.5	3.7	13.8	4.4		0.55	0.04	0.79	0.03
LS IV –14° 116 <sup>†</sup>	-154.0	1.0	8.15	0.05	0.66	0.14	0.24	0.02	-42.5	6.8	21.2	2.7	0.1	2.9		-0.35	0.06	0.85	0.03

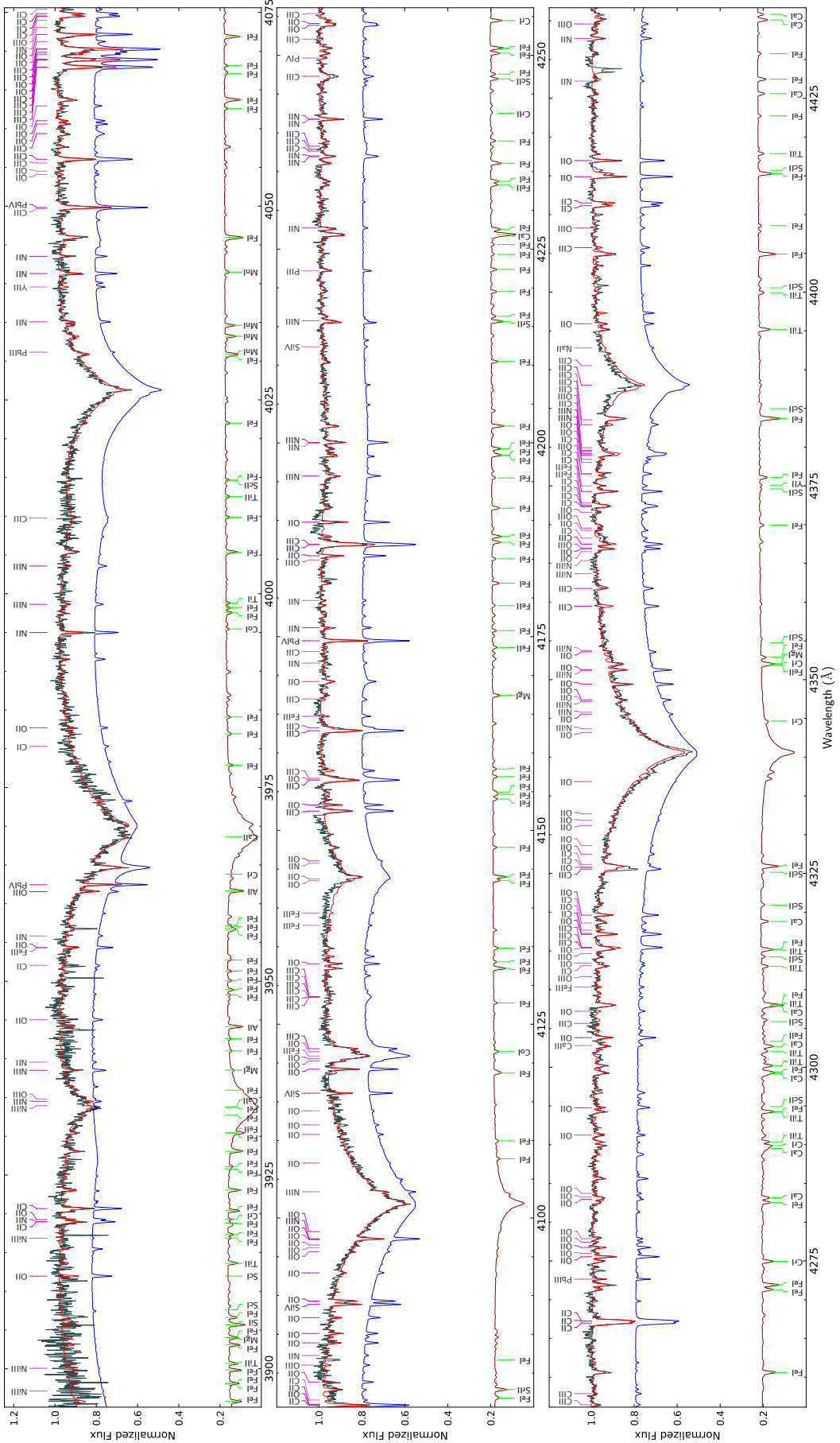


Fig. B.1: HRS spectrum of EC 22536–5304 (grey) and the combined (red) and individual models.

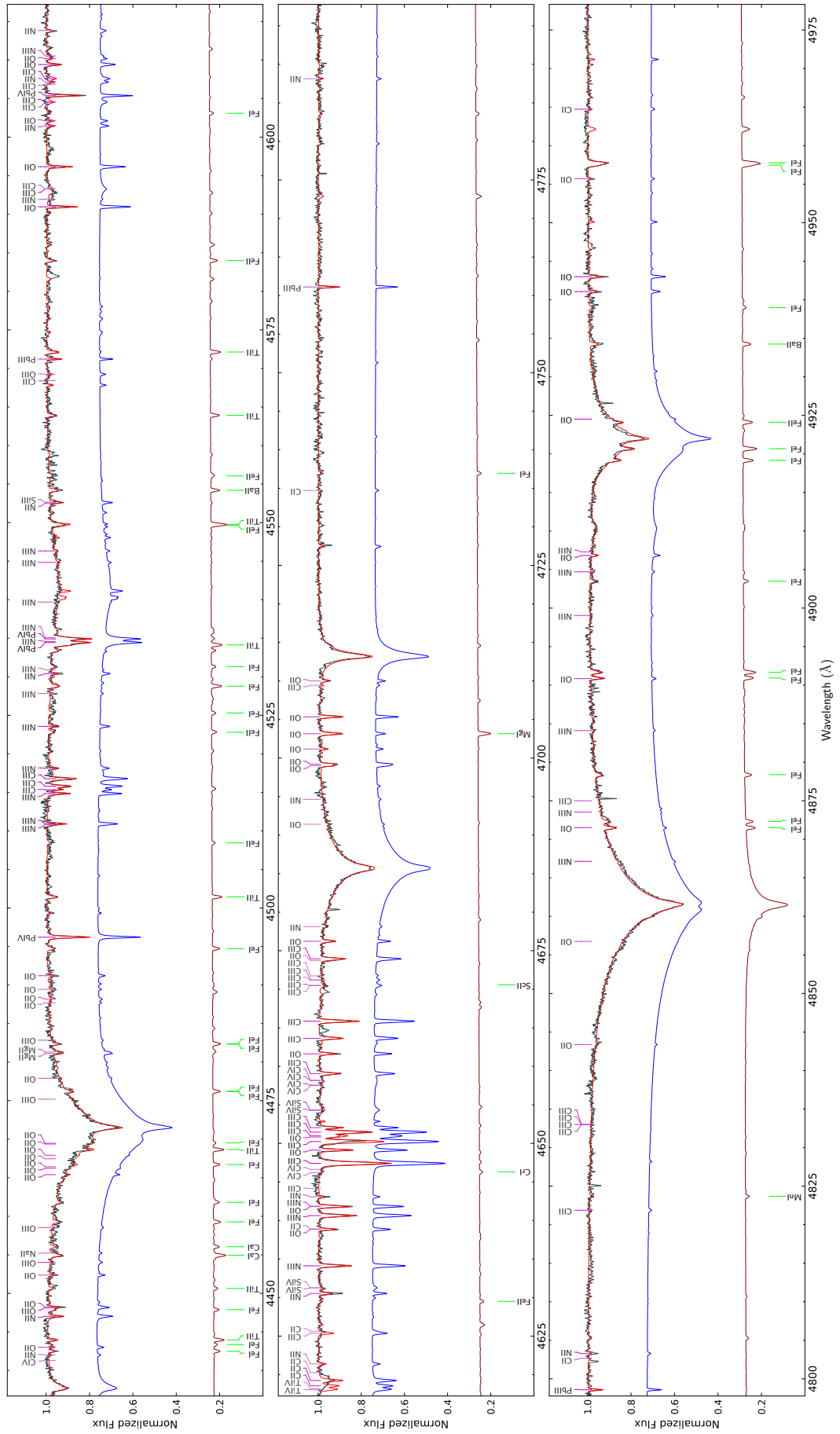


Fig. B.1 (continued): Blue HRS spectrum of EC 22536–5304 (grey) and the combined (red) and individual models.

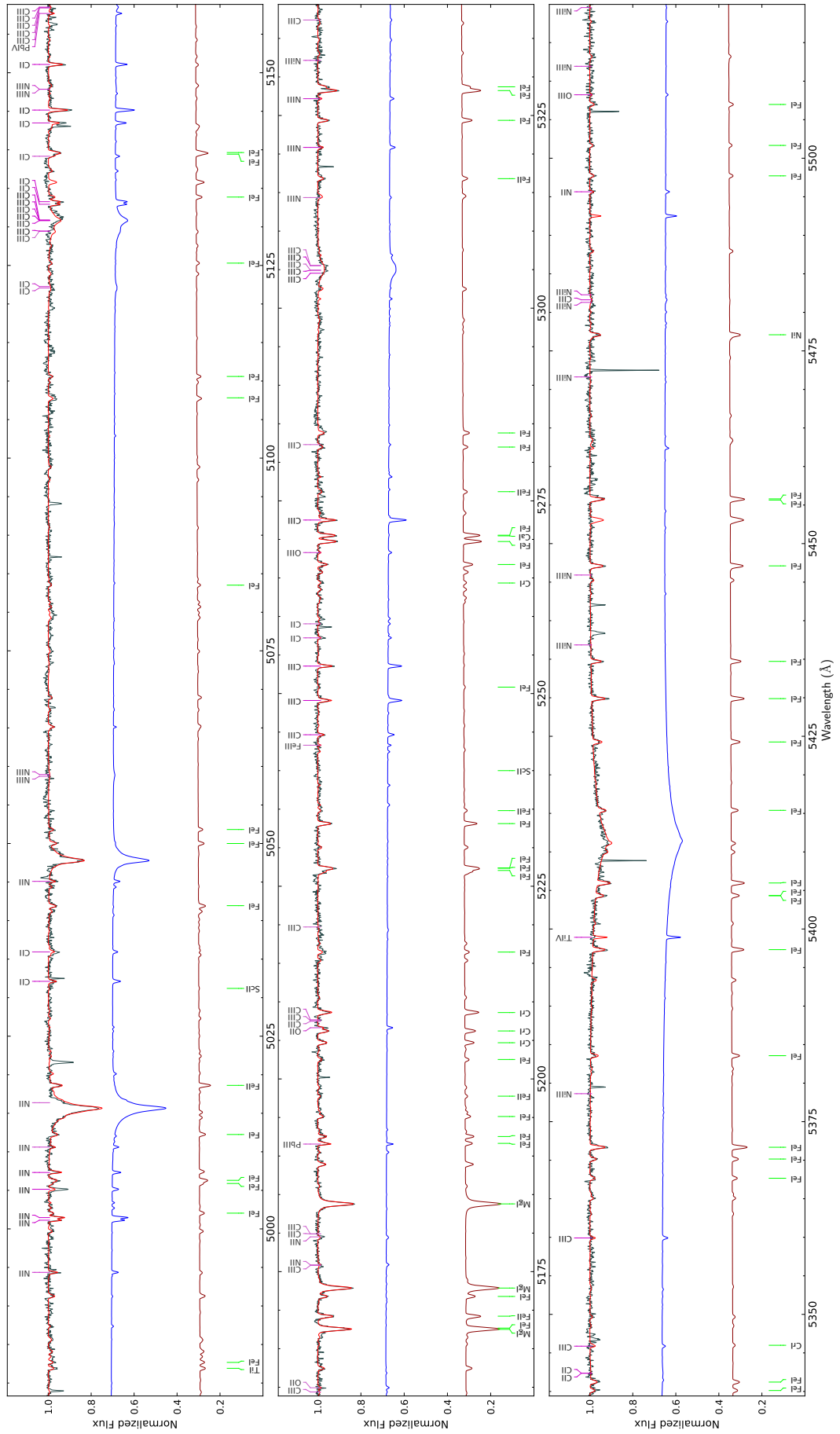


Fig. B.1 (continued): Blue HRS spectrum of EC 22536–5304 (grey) and the combined (red) and individual models.



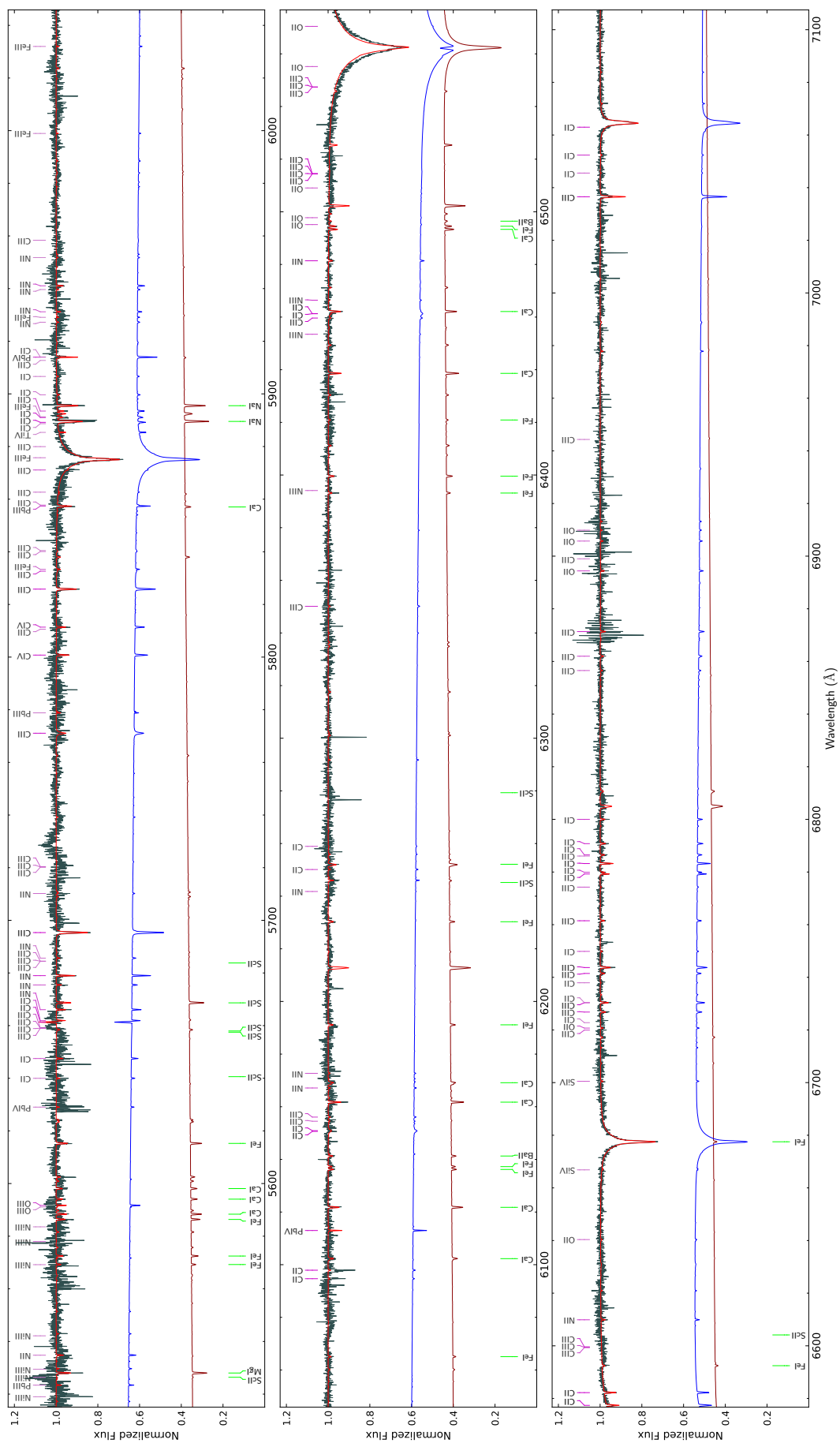


Fig. B.2: Red HRS spectrum of EC 22536–5304 (grey) and the combined (red) and individual models.

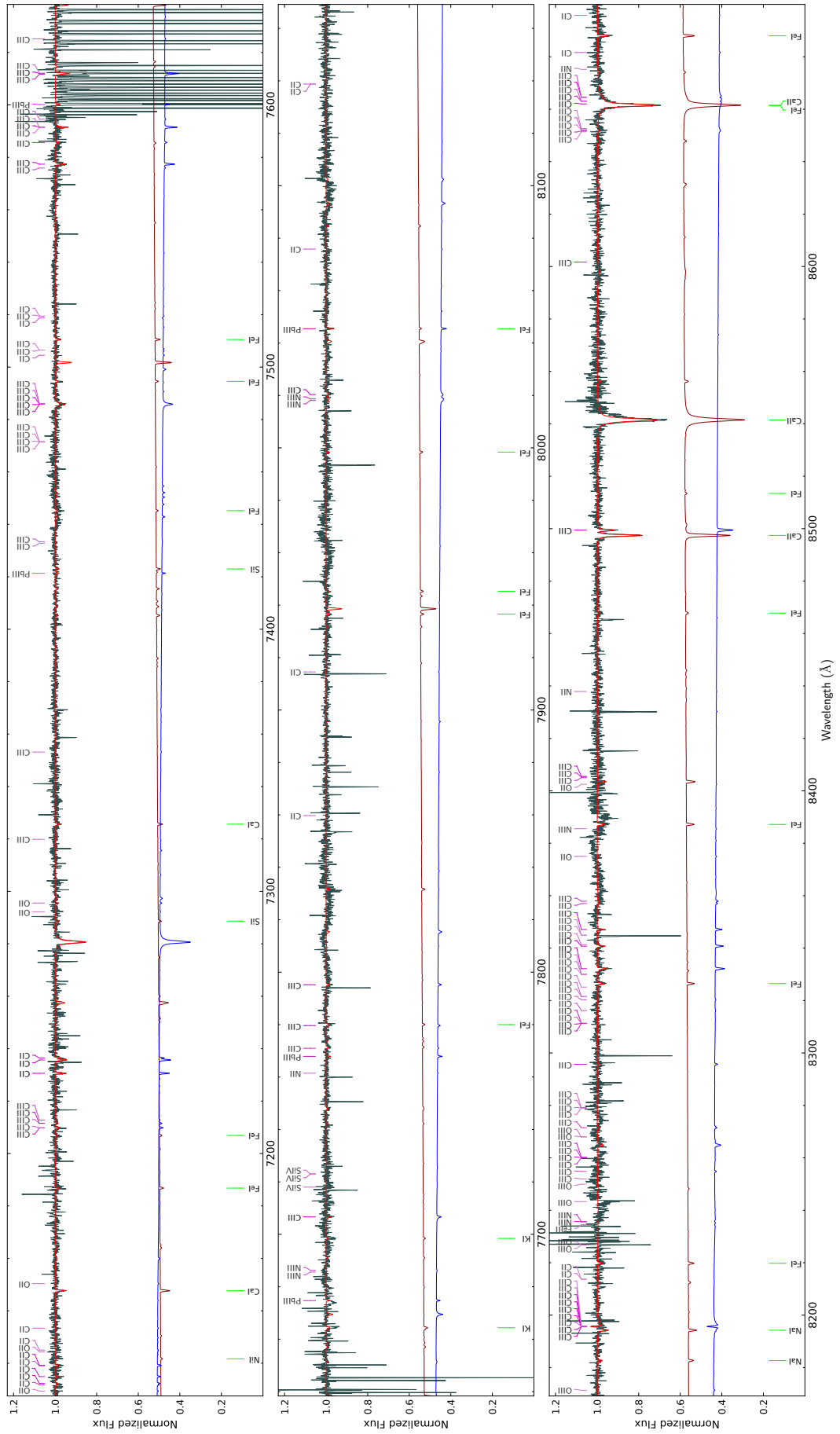


Fig. B.2 (continued): Red HRS spectrum of EC 22536–5304 (grey) and the combined (red) and individual models.

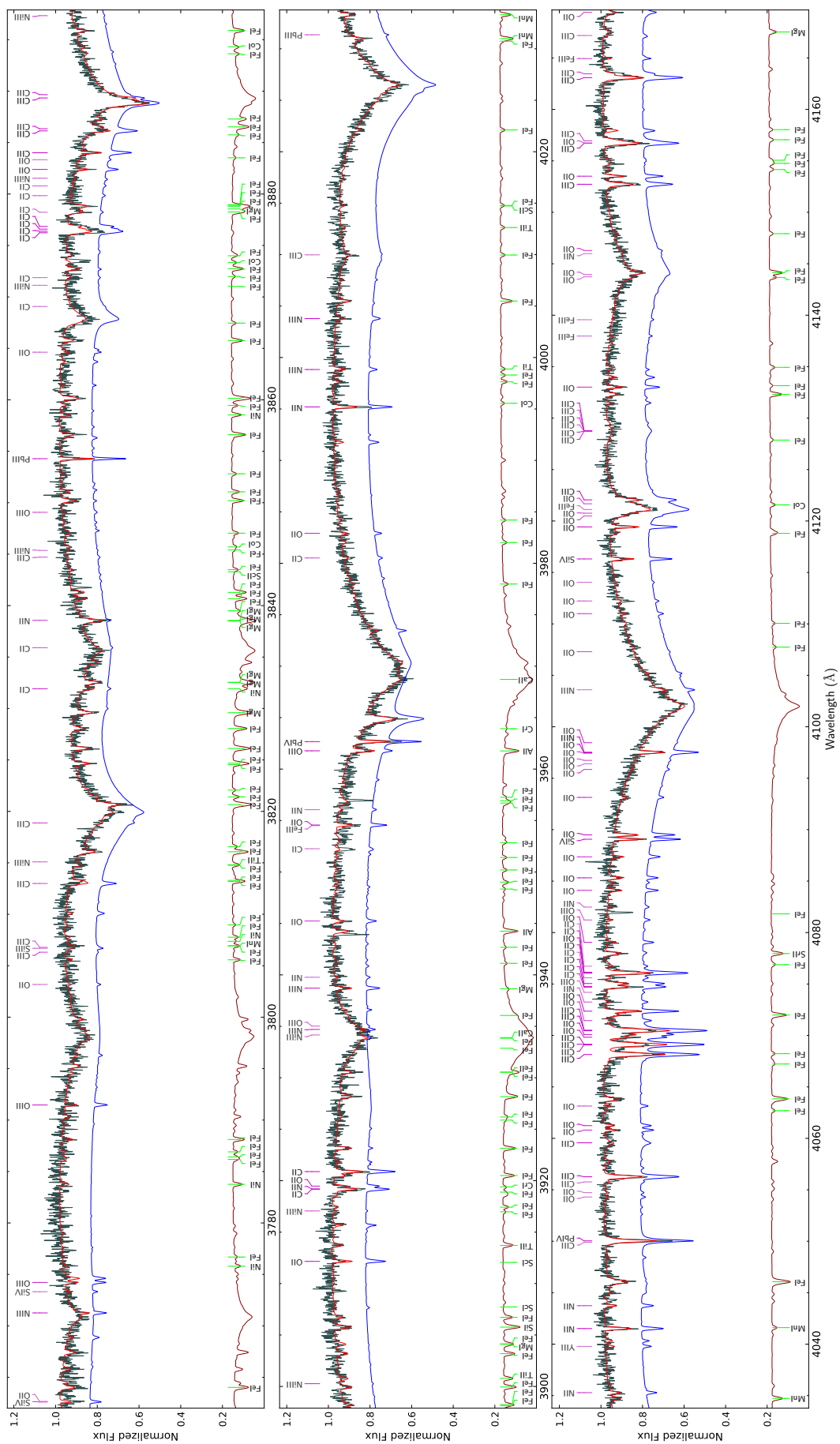


Fig. B.3: Blue UVES spectrum of EC 22536–5304 (grey) and the combined (red) and individual models.

Article number, page 20 of 23



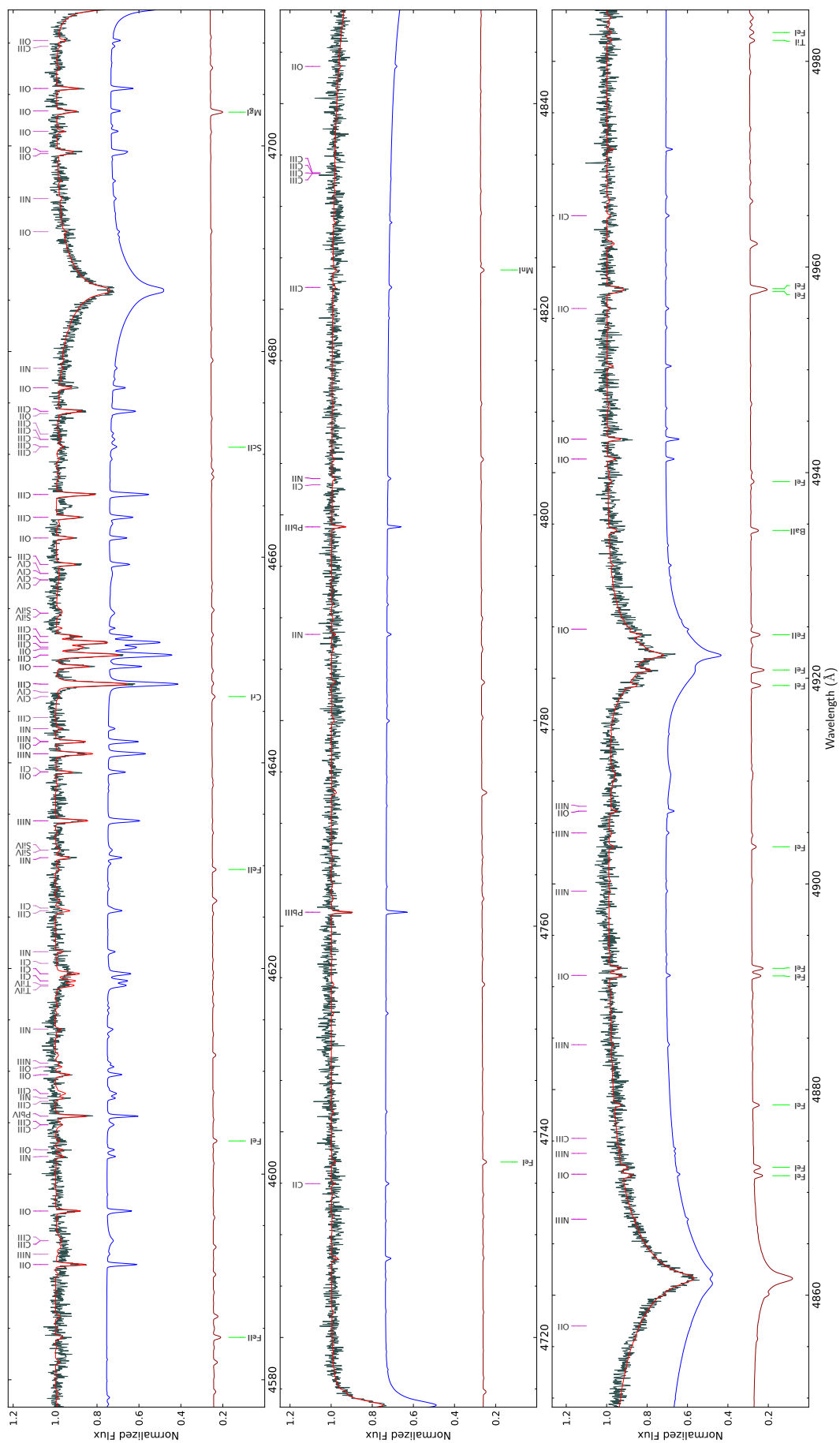


Fig. B.3 (continued): Blue UVES spectrum of EC 22536–5304 (grey) and the combined (red) and individual models.

Article number, page 22 of 23

Article number, page 23 of 23